UNIVERSIDADE DE LISBOA
FACULDADE DE CIÊNCIAS
DEPARTAMENTO DE FÍSICA

Massively Parallel Transmit Arrays at 7T: Innovative Array Elements and Geometries

José Nuno Azeredo Gomes Teixeira

Mestrado Integrado em Engenharia Biomédica e Biofísica
Perfil em Radiações em Diagnóstico e Terapia

Dissertação orientada por:
Dr. Ir. A.J.E. Raaijmakers
Dr. Rita Nunes

2016

Acknowledgements

I would like to thank the Erasmus+ scholarship for the funding provided without which my stay at the University Medical Centre of Utrecht to develop this project wouldn't have been possible.

I would also like to thank the University Medical Centre of Utrecht, specially the 7 Tesla research group for accepting me and allowing me to develop this project in their facilities as well as for providing me housing.

A last special thanks is in order to all my supervisors, co-workers, friends and family members for supporting me throughout this period of time.

Abstract

Working on ultrahigh-field Magnetic Resonance Imaging (MRI), namely with magnetic fields of 7 Tesla and higher, has increasingly demonstrated improvement in imaging performance when compared to lower magnetic field strengths, of 1.5 or 3 Tesla, due to an increase in obtained Signal to Noise Ratio (SNR). However, this improved performance was not applicable to all imaging modalities and it was until recently not achieved for objects located deep inside the human body (e.g. prostate, cardiac). Nonetheless, a significant improvement of intrinsic SNR for prostate imaging has recently been demonstrated [1].

One of the main reasons why this demonstration was not easily achieved is that with higher magnetic field strengths, the wavelength of the radiofrequency (RF) fields decreases to numbers comparable to the dimensions of small body structures located deeply inside the human body, causing interference patterns in the MR images due to B_1^+ field (RF field) inhomogeneity.

Additionally, RF exposure that comes hand to hand with MR imaging causes tissues to heat like in a microwave oven and at ultrahigh field strengths, this phenomenon becomes more pronounced when in comparison to lower fields. Associated with this heating at ultrahigh field strengths, a challenge that remains is the higher Specific Absorption Rate (SAR) levels which need to be kept under very strict thresholds. Heating is generally regulated by limitation of the SAR values, i.e. the RF power deposited per unit tissue mass. Currently, the power restrictions for ultrahigh field body imaging are much more stringent than at lower field strengths.

Body imaging at 7 Tesla is mostly performed using surface arrays with both receive and transmit capabilities (transceiver arrays). High SAR levels usually occur predominantly directly below the elements of the array. Currently, the maximum number of array elements is eight on most multi-transmit systems. It is possible that a drastic increase in the number of elements may reduce the SAR levels considerably due to the energy being distributed over more channels. This approach is called 'massively parallel transmit'.

Throughout this project, undertaken at the University Medical Centre of Utrecht (UMCU) facilities, numerical simulations were used to explore potential antenna designs for body imaging using massively parallel transmit technology by analysing the simulated transmit field (B_1^+) field and mass averaged SAR distributions and its ratio, as well as SNR levels. As a finishing step, the best performing geometry simulation-wise was built and tested as a transceive array.

A suitable candidate for a 'massively parallel transmit array' was identified during the course of the simulation step of this project by using an altered version of the fractionated dipole antenna as an array element. The array's performance, taking into account both transmit and receive efficiency, was noticeably better than the state of the art surface array consisting of an 8-channel fractionated dipole array. This array was built and submitted to some initial proof of concept tests in the scanner.

Keywords: RF excitation, transceive, far-field antennas, multi-channel, parallel transmit, B_1^+ shimming, SAR, SNR.

Resumo

O trabalho desenvolvido com ressonância magnética de campo ultra elevado, nomeadamente campos magnéticos de 7 Tesla e superiores, tem demonstrado melhorias no desempenho de imagem quando comparado com intensidades de campo menores (1.5/3 Tesla) devido ao incremento intrínseco da razão sinal-ruído (SNR). Embora seja esta a tendência geral, este aumento no desempenho não é linearmente aplicável a todas as estruturas do corpo humano, tanto que, não tinha sido atingido até recentemente para estruturas localizadas em profundidade no corpo humano (e.g. próstata, coração). Contudo, melhorias significativas no SNR intrínseco em imagiologia da próstata foram também recentemente atingidas e demonstradas [1].

Uma das principais razões pela qual esta demonstração não foi facilmente alcançada prende-se com o facto de que com o aumento de intensidade do campo magnético, o comprimento de onda dos campos de radiofrequência (RF) diminui para valores comparáveis às dimensões das pequenas estruturas localizadas no interior do corpo humano que se pretende visualizar, o que causa padrões de interferência nas imagens adquiridas devido à heterogeneidade do campo B_1^+ (campo RF). Para combater este efeito, é normalmente utilizada uma técnica denominada de *Parallel Transmit* cujo efeito é mais relevante quando a excitação RF é efetuada por um número elevado de canais e consiste em manipular a fase e a amplitude de cada canal para que se consigam diminuir os padrões de interferência na zona que se pretende visualizar. Esta técnica é já comummente utilizada em várias situações, não só em campos ultra elevados como também em intensidades de campo inferiores.

Para além desta questão, a exposição aos campos RF que necessariamente se encontra associada a exames de ressonância magnética (MR), causa aquecimento dos tecidos tal e qual um forno micro-ondas e quanto mais alto o campo magnético de trabalho, mais pronunciado se torna este fenómeno. Trabalhando a uma intensidade de campo de 7 Tesla, este aquecimento torna-se uma questão ainda mais preocupante do que quando se trabalha a campos de intensidade mais reduzida. Associado a este aquecimento aquando da utilização de campos ultra elevados, agrava-se o desafio de minimizar os níveis de *Specific Absorption Rate* (SAR). O aquecimento é regulado pela limitação deste parâmetro, que representa a potência RF depositada por unidade de massa de tecido irradiado. Atualmente, as restrições de potência aplicadas a imagem em campos ultra elevados são muito mais estritas do que a campos magnéticos mais baixos. Quando limitando os valores de SAR é importante ter em conta não só a potência dissipada no corpo inteiro como também a potência dissipada localmente em certas porções de massa de tecido, nomeadamente a cada 10g.

As imagens a 7T são maioritariamente efetuadas utilizando *arrays* de superfície que funcionam como transmissor e recetor. Níveis altos de SAR ocorrem predominantemente diretamente abaixo dos elementos usados nestes *arrays*. O número de elementos na maioria dos sistemas de multi-transmissão, atualmente, é normalmente oito, número que já permite uma boa utilização das técnicas de *Parallel Transmit*. Contudo, um aumento drástico no número de elementos utilizados pode resultar num controlo mais eficaz das interações do campo B_1^+ e numa diminuição considerável dos níveis de SAR devido à energia fornecida ao sistema ser distribuída por mais canais. Esta abordagem que consistente no aumento do número de canais foi então apelidada de de *'massively parallel transmit'*.

Tendo identificado os *'massively parallel transmit'* como uma potencial solução para alguns dos problemas encontrados para ressonância magnética de campo elevado é necessário analisar morfologicamente e eletricamente possíveis soluções para a criação de um sistema deste género. Em primeira instância, é importante referir que trabalhando a 7 Tesla de intensidade de campo com a finalidade de visualizar estruturas localizadas no interior do corpo humano, é necessário trabalhar com sistemas de excitação RF que trabalhem em *far-field*, nomeadamente antenas RF não

ressonantes, ao contrário do que acontece com as estruturas ressonantes normalmente utilizadas a campos magnéticos mais reduzidos (e.g. *birdcage coil*). Posto isto, é necessário, em primeira instância, identificar os tipos de antenas a testar como elemento de um *'massively parallel transmit array'*.

Um outro grande problema de utilizar vários canais no sistema de excitação RF é o facto de a potência fornecida num certo canal poder ser refletida de volta para o sistema de alimentação ou até dissipada nos restantes canais, perdendo-se assim energia que deveria ser utilizada para excitação. A questão da dissipação de potência entre canais pode ser contornada colocando os diferentes elementos em posições cuja interferência com os restantes seja mínima e a potência dissipada seja reduzida para valores aceitáveis. Além disso, alguns elementos são intrinsecamente menos propícios a interações inter-elemento tal como é o caso dos dipolos, elemento este, sob cujo projeto incidirá fortemente. Já a minimização da reflexão de potência de volta para o sistema de alimentação é conseguida igualando a impedância de entrada de cada elemento com a impedância da fonte.

Não só com o tipo de antena a usar se prende a complexidade do problema, também o seu posicionamento dentro do *array* é de extrema importância, principalmente quando se trata antenas *loop*. Posto isto, de modo a correta e eficazmente avaliar o desempenho de cada um dos potenciais candidatos a um bom *'massively parallel transmit array'* é necessário recorrer a ambientes de simulação eletromagnética de modo a ter uma fiel estimativa do desempenho de qualquer configuração testada. Recorrendo a simulações electromagnéticas para a análise de desempenho é possível analisar um grande número de diferentes elementos e configurações espaciais num relativamente curto espaço de tempo. Sendo assim, será possível cobrir um grande numero de diferentes *arrays* e consequentemente ter um melhor conhecimento da influência dos fatores não constantes na performance dos mesmos.

No decorrer deste projeto, desenvolvido nas instalações do *University Medical Centre of Utrecht* (UMCU), todas as simulações foram efetuadas com o intuito de explorar potenciais *designs* de antenas para imagem usando esta abordagem, analisando o campo de transmissão (B_1^+), as distribuições de SAR e o rácio entre as duas quantidades, assim como os níveis de SNR. O SNR é também um fator importante na análise do desempenho de um dado *array*, pois embora seja de extrema importância minimizar o aquecimento devido à potência dissipada nos tecidos é também importante assegurar que o sinal recebido pelo sistema de receção não perca intensidade, garantindo que se mantém a qualidade das imagens obtidas quando se utilizar este sistema.

Tendo simulado várias configurações possíveis para um *'massively parallel transmit array'*, foi necessário proceder a uma cuidadosa análise de todos os fatores que tornam um sistema de excitação fidedigno, nomeadamente a intensidade do campo B_1^+, os níveis de SAR local e o SNR. Resultante desta análise, foi identificada uma configuração que obtenha um desempenho superior a todas as outras. Esta configuração possuí como elementos uma variante da '*fractionated dipole antenna*' e o seu desempenho, tendo em conta tanto a sua eficiência de transmissão como de receção, é claramente superior à configuração atualmente considerada o estado da arte que consiste num *array* de oito '*fractionated dipole antennas*'.

Não só de simulações é composto este projeto, em última instância, a configuração que obteve o melhor desempenho entre todas as simuladas, foi construída e montada (cada elemento terá de ter a sua impedância natural alterada de modo a minimizar a potência refletida de volta para o sistema de alimentação) num *array* real.

Estando o *array* pronto, foi ligado ao sistema de *parallel transmit* do *scanner* presente nas instalações do UMCU de modo a efetuar alguns testes de prova de conceito para que se pudesse comprovar a viabilidade de um *'massively parallel transmit array'* enquanto sistema de transmissão e receção RF.

Contents

List of Figures

List of Abbreviations

B_1^+ - RF transmit field
MR - Magnetic Resonance
MRI - Magnetic Resonance Imaging
pSAR10g - Maximum Local 10g Averaged SAR
RF - Radiofrequency
ROI - Region of Interest
SAR - Specific Absorption Rate
SNR - Signal to Noise Ratio
SSAD - Single-side Adapted Antenna
UMCU - University Medical Center of Utrecht

1 Underlying Concepts

This document will be structured into a logical path to fully understand the train of thought applied through the course of the project. All the following steps are displayed in a way that allows the reader to fully distinguish between preliminary work, included in the section 3, from the main focus of the project which is only addressed to specifically in section 4.

In a first step, all relevant background information about previous work developed on the topic will be briefly described in section 2, in order to better comprehend the issue at hand. Having an objective clearly identified, a second step of preparation is explained, all methods and simulation protocols used to achieve results ready for analysis and comparison are described in detail in section 3. Furthermore, in section 4, the third and final step, consists of presenting, analysing and discussing all results obtained with the help of the methods and protocols described in section 3.

Although for an expert in the field, the previously described structure would suffice,in order for any reader to fully understand the proposed workframe for this project, several theoretical concepts and techniques must be further explained and kept in mind to better understand the goal of improving transmit and receive performance at high field imaging of deeply located structures while reducing SAR levels.

1.1 Magnetic Resonance Imaging

Magnetic resonance imaging as a medical tool is a rapidly increasing area due to its excellent contrast potential and accuracy for most of the human tissues. Also, although it is a technique that has been used for over 30 years there is still no empirical trace of potential long term side-effects it might induce on the subjects. It is, very broadly speaking, based on the behaviour of the magnetization vector of a given set of precessing protons after being excited by controlled RF pulses [2].

The typical MRI system consists of a myriad of components [3] which include the RF excitation system. The main magnetic field, usually defined as B_0, defines the atoms' Larmor frequency which is the frequency at which the RF excitation system must operate [2], in order for resonance to occur. For this project the working B_0 field will be of 7 Tesla which corresponds to a working Larmor frequency of approximately 298MHz and an effective wavelength inside the human body of about 15 cm.

1.2 Transmit/Receive Regime

RF surface arrays are used as both the transmitter and the receiver in an MRI system aiming for a multichannel local array approach.

As already mentioned, there is a plethora of available geometries for the elements used in surface arrays. Although in this specific project several geometries and array elements are used, the goal to keep the arrays in a transceive regime is kept constant throughout the study.

This means the arrays must be able to transmit the excitation pulses and receive the resulting responses of the excited tissues. Most of the information relevant to assess the transceive capabilities of a given array are stored in the B1 field generated by the array when driven with a given power. The B1 field components (Equation 1) are of a huge importance for tissue excitation and signal received performance.

$$\begin{aligned} B_1^+ &= \tfrac{B_{1x}+iB_{1y}}{2} \\ B_1^- &= \tfrac{(B_{1x}-iB_{1y})^*}{2} \end{aligned} \tag{1}$$

When building a surface array as it is proposed in this project, it is important to keep in mind that B_1^+, the positively rotating RF field, is directly related to the excitation performance and that B_1^-, the negatively rotating RF field, as it will be explained in section 1.8, is of great importance when calculating the maximum achievable SNR of an array[4].

1.3 Far-field Antennas as array elements

Most of the commercial lowfield MRI coil setups are designed as near field. These designs are generally tuned to resonate at the operating frequency in order to generate a large radiofrequency (RF) field in the near field region. This can be used as an advantage when the structures to be imaged are located inside this near field region, i.e. in 3T and lower MRI setups. However, in MRI, there is a general tendency to aim for higher B_0 fields due to the higher SNR it provides and the operating Larmor frequency of the RF fields necessary to excite the imaging objects also increases linearly according to Equation 2.

$$f = \frac{\gamma}{2\pi} B_0 \tag{2}$$

where f is the frequency, γ is the single proton gyromagnetic ratio (approximately 42.6 MHz/T) and B_0 the external magnetic field intensity.

Consequently, the increase in frequency leads to a reduction of the operating wavelengths placing many structures of interest out of the near field region boundaries. In order to obtain effective field penetration for the mentioned structures far-field antennas must be explored. These antennas are designed such that the cross product of the generated **E** and **B** (called the Poynting vector) is directed towards the target location, in order to emit the electromagnetic wave into the medium more efficiently, and that their strong near-field component does not enter the superficial conductive tissues. Several of these far-field antennas have been discussed and tested in previous publications [5].

1.4 Numerical Simulations - FDTD Method

Numerical simulations seek to implement solvers which are an efficient solution to solve the Maxwell's equations associated with each new coil array to be tested. There are several solvers currently used but throughout this project all simulations will be performed using the Finite-difference Time-domain (FDTD) solver package of Sim4Life (Zurich MedTech, Zurich, Switzerland).

The FDTD method consists in a numerical analysis technique widely used to simulate electrodynamic systems by finding the approximate solution to the associated set of differential equations. Since it is a time-domain method, FDTD allows the user to analyse the system in a broad range of frequencies as well as incorporate non-linear materials in the models to be tested.

This method discretises the time dependent Maxwell's Equations in their partial differential form [6] using central-difference approximations to the space and time partial derivatives. As a result, the obtained and solved finite-difference equations generate a mesh of cells corresponding to locations within the subject with the value of all the **E** (Electric) and **B** (Magnetic)-field components of the RF field at every cell.

1.5 Parallel Transmit and B_1^+ shimming

Most of the work put into improving image quality at high field strength has been focused towards driving several independent channels with different phases and amplitudes in order to control and manipulate the interactions between the propagating B_1 fields from the different channels. This technique is known as Parallel Transmit and it has to be applied to any antenna arrays in order to further improve performance. To implement parallel transmit, the weightings to apply to each channel must be calculated by performing B_1^+ shimming.

In any multi-channel MRI system the B_1 field is generated as a linear superposition of the field efficiencies $\mathbf{S}_{B1}$ of each active channel [7]. For two channels it can be represented by the following equation:

$$B_1(x) = \mathbf{S}_{B1}(x) \cdot \mathbf{W} = (S_{B1,1}(x)\ S_{B1,2}(x)) \cdot \begin{pmatrix} W_1 \\ W_2 \end{pmatrix} \tag{3}$$

where $\mathbf{W}$ is the vector containing the weighting complex values for each channel, x the position in space and $\mathbf{S}_{B1}$ is usually acquired from B_1 mapping techniques [8]. As stated earlier, the weightings that should be applied to each channel can be obtained by performing B_1^+ shimming in the region of interest

Obtaining the shim values W_i can be presented as an optimization problem as in 4 whether the objective is to increase homogeneity or purely increase B_1^+ intensity in the region [9].

$$\mathbf{W} = \arg_{\mathbf{W}}\min\{||\mathbf{S}_{B1}\mathbf{W} - \mathbf{m}_{targ}||^2 + R(\mathbf{W})\} \tag{4}$$

where $\mathbf{m}_{targ}$ is the target matrix representing the desired outcome for the B_1^+ distribution and R($\mathbf{W}$) denotes a general regularization term that can be set to e.g. constrain SAR levels.

1.6 Specific Absorption Rate

As previously mentioned, one of the key concerns in multi-transmit MRI technology is the amount of energy that is deposited during the RF excitation of the subject which is usually quantified as the Specific Absorption Rate. SAR is analysed in two different manners, it can be assessed as the global SAR, which is the SAR averaged throughout the whole body or assessed as the local SAR that is averaged throughout a fixed mass (usually 1g or 10g of mass).

The current solution for evaluating SAR deposition is to use EM simulations like FDTD to calculate the electromagnetic field components.

Furthermore, it is necessary to understand how SAR values are obtained from E-field values [10]:

$$SAR(x) = \frac{\sigma(x)}{2\rho(x)}|E(x,t)|^2 \tag{5}$$

where σ is the electrical conductivity of the cell being evaluated, ρ the density and E is the total E-field vector at the x location.

Once these point SAR values have been calculated, as mentioned before, it is possible to integrate them over a given volume in order to obtain local SAR values averaging each element over 10g of tissue according to the following operation:

$$SAR(x) = \frac{1}{V}\int \frac{\sigma(x)}{2\rho(x)}|E(x)|^2 dV \tag{6}$$

where V is the volume encompassing the 10g of tissue.

With the Sim4Life SAR calculation tools it is possible to generate 10g Averaged SAR matrices from the values of the simulated electric field. This is particularly important since the International Electrotechnical Commission (IEC) guidelines require, not only the SAR correspondant to the total absorbed power (Global SAR), but also 10g Averaged Local SAR to be below a certain threshold[11] therefore imposing constraints on imaging parameters and/or scanning speed.

1.7 Scattering Parameters and Power Reflection

Scattering-Parameters or S-Parameters (usually organized in matrices) are a more convenient way to describe electrical behaviour of linear electric networks undergoing electrical stimuli at radio and microwave frequencies than the commonly used currents and voltages. S-Parameters essentially assess whether the travelling currents and voltages are affected by discontinuities in the electrical network caused by the structure's geometry, presence of other conducting elements, presence of lumped elements (inductors, capacitors, resistors), etc. in the full network.

This way, for each driven port, it is possible to evaluate the ratio at which the power is lost through all discontinuities, more specifically the power lost in the element being driven itself and the power lost to other neighbouring elements. Thus we can differentiate inside the S-Parameters matrix, values for each combination of elements, defining two important subsets: S_{nn} as the S-Parameters related to the way the elements of the structure lose power themselves mainly by reflecting current at their driving point and S_{nm} related to the way each element loses power by interaction with the remaining elements. For example, for the case where the system is only driven at 2 ports see 7.

$$\begin{pmatrix} b_1 \\ b_2 \end{pmatrix} = \begin{pmatrix} S_{11} & S_{12} \\ S_{21} & S_{22} \end{pmatrix} \begin{pmatrix} a_1 \\ a_2 \end{pmatrix} \tag{7}$$

where a_n and b_n are the input signal and the output signal for the n^{th} port respectively.

The power lost by interaction with the remaining elements is not easy to counter and it is dependant on spatial distribution and element geometry. Trying to minimize this effect is a common step in designing an array with elements that tend to have very high power losses to neighbouring elements, as is the example of the loop antenna. This minimization process is usually referred as the decoupling process since the power losses are commonly referred to as the coupling of the elements.

The power reflection happening at the driving point of the element is usually caused by a bad matching to the impedance of the energy source system which works at 50 Ω. In order to counter this power reflection it is necessary to undertake a process referred to as impedance matching.

1.8 Signal to Noise Ratio

Throughout this study, the receive performance of all arrays was evaluated in terms of potential SNR. These potential SNR calculations, performed with Sim4Life, are independent of any shim parameters, local spin density since unity spin density and unity flip angle are assumed. Using this method, for any given input power every array will only have one potential SNR value which is dependent on field strenght, noise and coupling of the individual elements. The SNR can be calculated with the information about the noise covariance matrix and the RF field normalized to the input current. Roemer et al. [12] describes a method to obtain the potential SNR for a given multichannel array using the noise covariance matrices. SNR calculations are a complex topic and beyond the scope of this project, nonetheless, a simplistic approach to the method consisting of the core equations used will be described in this section, starting with Equation 8 that allowed the calculation of the noise covariance matrices for every simulated array.

$$R_{ij} = \frac{1}{I_i * I_j} \sum_{n=1}^{n} \sigma(n).\mathbf{E}_i^*(n).\mathbf{E}_j(n).\Delta V(n) \tag{8}$$

where R_{ij} is the noise covariance matrix entry for ports i and j, I the current on the respective port i or j, $\sigma(n)$ the electrical conductivity at voxel n, $\mathbf{E}(n)$ the E-field vector contribution for voxel n from port i or j, respectively and $\Delta V(n)$ the volume of voxel n.

Having the noise covariance matrix calculated, the potential SNR can be obtained following Equation 9

$$SNR(n) = \sqrt{\mathbf{b}_1^*(n).\mathbf{R}^{-1}.\mathbf{b}_1(n)} \tag{9}$$

with $\mathbf{b}_1 = \mathbf{B}_1^-/\mathbf{I}$, where $\mathbf{b}_1$ is the column vector (n^o of ports x 1) with the receive sensitivities for all ports, $\mathbf{R}$ the full noise covariance matrix and n the number of voxels.

With this last equation it is possible to calculate the potential SNR possible for a given array, allowing us to have a way of comparing the receive performance of all simulated arrays.

1.9 Matching and Decoupling

In sequence to the topic introduced alongside the Scattering Parameters in section 1.7, it is of great importance to correctly minimize the power reflection that occurs normally in any set of multichannel antennas.

Matching is the name given to the process of bringing the impedance of a given antenna to the same value as the input impedance of the feeding power supply of 50 Ω. This matching is obtained by adding lumped elements to the antenna in such a way that the total circuitry network has a natural impedance of 50 Ω minimizing power reflection at the driving point.

Coupling to different elements of a given array also needs to be minimized and that process is called decoupling. Coupling happens when two antennas "see" each other electrically and part of the input power they receive is dissipated in the other antenna. This coupling is influenced by spatial placement and geometry of the antennas, being that some antenna shapes are more prone to coupling than others.

Working with dipoles doesn't usually lead to inter-element coupling so throughout this study, all dipole arrays were assumed to have negligible coupling. When working with loops, the coupling was minimized by spatially overlapping the neighbouring elements. The idea behind this method is to have the fields generated by the antennas to pass through the neighbouring antennas in different directions simultaneously and cancel the coupling effect forcing them to virtually not "see" each other electrically. This overlapping works better at an ideal length of overlap. To find the ideal overlap is the real challenge behind decoupling loops and it will be covered in section 3.

2 Introduction

In the commonly used surface arrays in lower field MRI (which were built as resonant structures), a higher quality factor of the resonance would result in higher resonating currents and consequently in higher B_1 field strengths. However, with these elements, the B_1 field increase was only noticeable in the near-field region resulting in a suboptimal performance of these elements for high field MRI. It has been shown [13] that for high field MRI, deeply located targets fall outside of this near-field region. This resulted in the introduction of far-field antennas as possible surface array elements to be used in high field MRI.

2.1 Multichannel Antenna Arrays: Loops and Microstrips

One of the first investigations regarding new antenna types for 7 Tesla MRI was done in 2005 and it tests the usage of three different multi-channel arrays, an 8-channel microstrip antenna arrays and loop arrays with 4 and 8 channels [14].The arrays tested in this study can be seen in Figure 1.

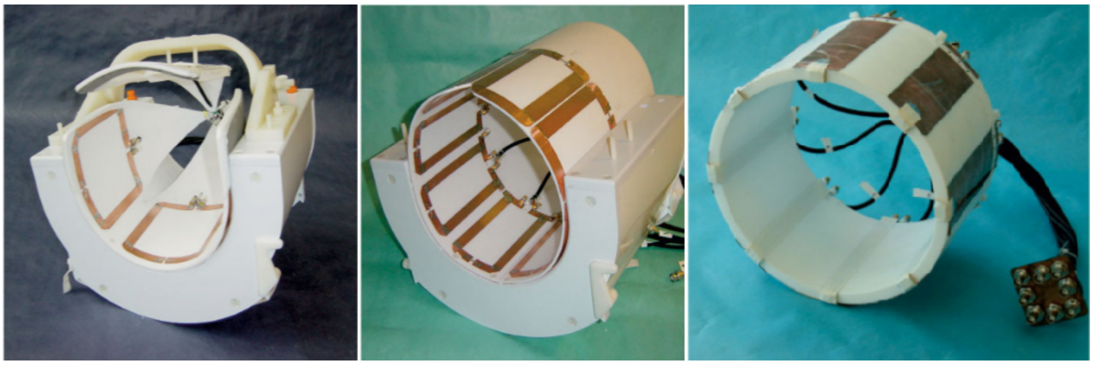

Figure 1: Arrays tested for local imaging at 7T. From left to right: 4-channel loop array; 8-channel loop array; 8-channel microstrip antenna array [14].

All arrays were tested in terms of ease of decoupling, B1 penetration, SNR and parallel imaging capabilities by exerting all necessary measurements and subject test. Initial studies like this one were a great step into backing up further researching the use of local multichannel antenna arrays that can hopefully eliminate the need for the use of large coils by acting both as transmitter as well as a receiver for high field MR, such as 7T. The short wavelength at this high field allows the individual coils to be decoupled from each other easily without needing to install complex decoupling networks. These multichannel setups also allow for higher freedom of phase and amplitude manipulation in the transmit mode that directly translate to a possible implementation of transmit SENSE or RF shimming which prove to be very useful when working at high field strengths as shown previously [15].

2.2 The SSAD Antenna

This perspective of using multichannel arrays in high field MRI resulted in promising insights about far-field antennas applied to 7 Tesla fields with the introduction of the dipole antenna. Knowing that the dipole antenna may have advantages over more conventional array elements when imaging deeply located elements, several studies have been conducted with this antenna as a starting point. It was first introduced as an array element in 2009 [16] and this work was later published as a full paper in 2011[5] by introducing the single-side adapted dipole antenna (SSAD)as in Figure 2.

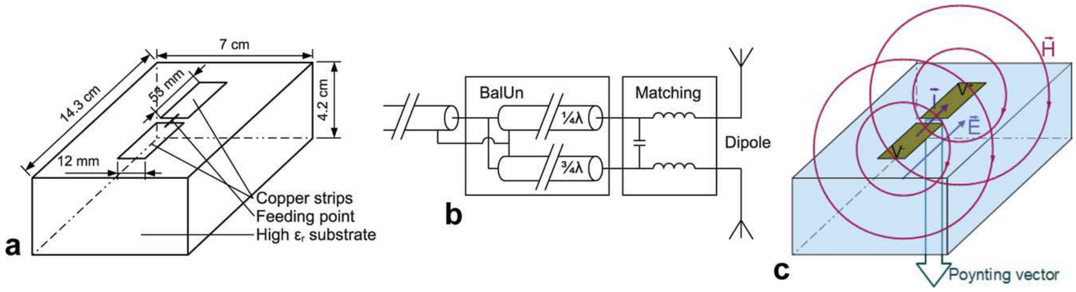

Figure 2: Single-side adapted dipole antenna: (a) schematic and example dimensions; (b) electric circuit schematic; (c) E-fields, H-fields and Poynting vector, which represents the directional energy flux density of an electromagnetic field [5].

The SSAD antenna was built as a dipole mounted on a ceramic substrate to keep the conservative E-fields associated with dipole antennas outside the subject tissue. The results were a larger signal penetration and a more homogeneous excitation/sensitivity pattern, particularly for higher field strengths.

At first, the dielectric substrate was thought to be essential to: (i)enclose the high conservative E-fields of the dipole antenna, avoiding high SAR levels; (ii)increase directivity towards the subject; (iii)match the transition from antenna to tissue.

However, in 2012, it was shown [17] that (ii) and (iii) were actually not true and good performance without the ceramic substrate was achievable. Also (i) was proved to be wrong in [18] with the introduction of the fractionated dipole antenna.

2.3 Loop arrays for cardiac imaging

Since the first studies regarding loop antennas at 7T, several other research groups followed the footsteps of using these multi-channel arrays for several different applications, namely cardiac imaging with loop arrays as is the case for the work developed with an 8-channel transceive array in the Berlin Ultrahigh Field Facility [19].

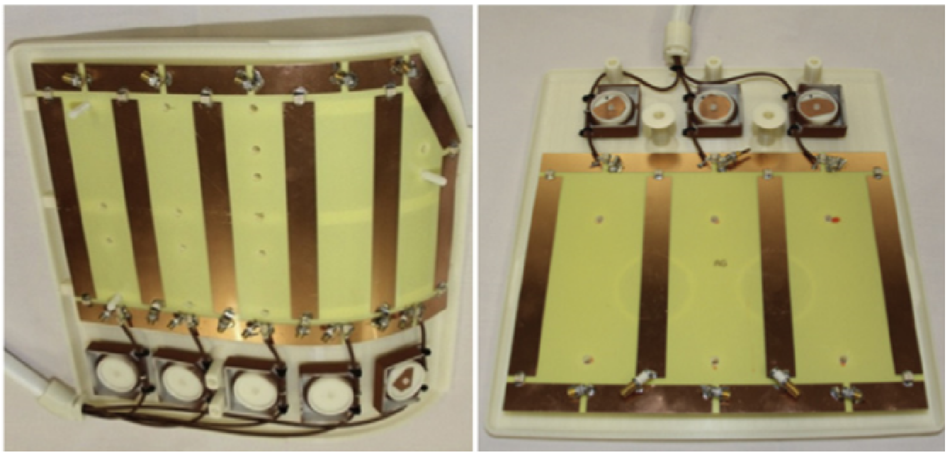

Figure 3: Final structure of the 8-channel dedicated loop surface array depicting the 5-channel top array (left) and the 3-channel bottom array (right) [19].

This study altered substantially the symmetry of a conventional loop array, adapting it for cardiac imaging purposes, the array is divided into a top and a bottom array where the first comprises of 5 loops with the left-sided loop bent to adapt to the torso morphology on the top array and 3 on the bottom array to be placed on the back of the subject as seen in Figure 3.

Before testing the array on volunteers, electromagnetic simulations were performed on a human model to estimate the maximum RF power levels possible to apply without exceeding the stipulated maximum SAR values. In the simulations the output of the amplifier was constrained at 30 W, leading to a local SAR limit of 7W/Kg for the 70Kg human model used.

The entire array undertook an element decoupling process with a body load in it resulting in acceptably low inter-element (maximum -11dB) and self-coupling (maximum -14 dB). Additionally, B_1^+ phase shimming was done for imaging in the volunteer tests to obtain the optimal field pattern for cardiac imaging.

This study demonstrated the feasibility of a dedicated multichannel array for cardiac MR using loop antennas as array elements. Several data acquisitions were done with this array using a 2D CINE FLASH technique and a clinically acceptable view of the heart was obtained with a rather uniform field intensity distribution (Figure 4). Once again, the results here obtained were expected to set in motion further research regarding RF coil technology for local surface array designs.

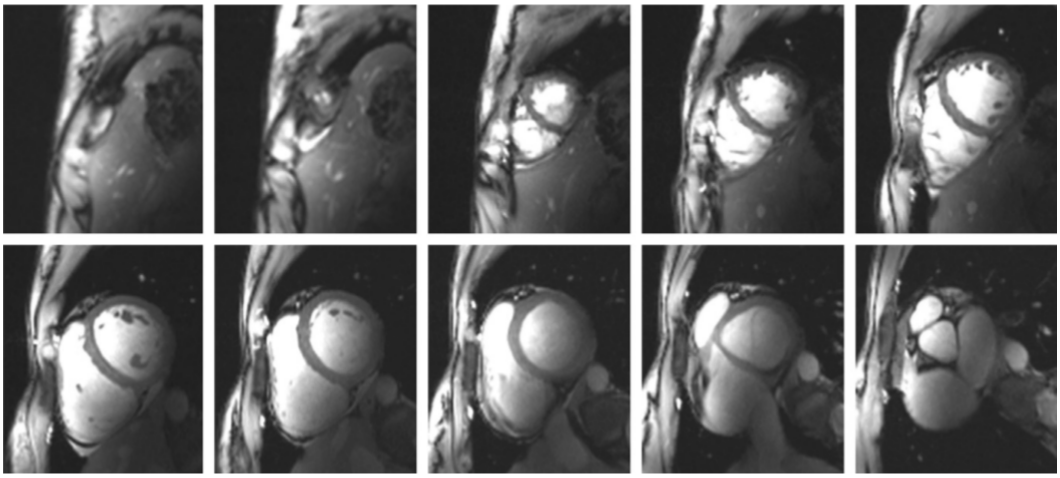

Figure 4: A set of 2D CINE FLASH acquisitions covering the entire heart using the dedicated 8-channel loop surface array where the expected increase in B_1 homogeneity is noticeable, granting a clear view of the heart [19].

2.4 A Performance comparison between Dipoles and Loops

The efficiency and reliability of the dipole antenna for imaging has already been explored at the UMCU by Raaijmakers *et al.* [20], while comparing it to a commonly used element, the loop coil . In that article electromagnetic insight into the general operating principles of dipole antennas is provided by an extensive series of simulation studies. More specifically, a series of basic simulation setups is used to show under what circumstances the dipole will emit its energy towards the imaging target.

For this study, several scenarios were simulated under the same circumstances in order to compare both elements. Loop coils with increasing diameter (5, 10, 15, 20 and 25 cm) and dipole antennas with increasing length (5, 10, 15, 20, 25, 30, 35, 40 and 45 cm)(Figure 5) were placed over a cubic phantom (ε_r=34, σ=0.4). Among other frequencies, tests were done for 298MHz (Larmor frequency at 7T) and conclusions were drawn regarding the performance of both elements with increasing depth. In Figure 6(left) a plot of the best performing elements in terms of maximum projection B_1^+ profiles over depth from the phantom surface into higher depths can be seen. It shows the best performing element and element length/diameter for each depth such that the following relationship seems to stand out: at shallow depths, loop coils perform better; at larger depths dipoles perform better.

As for Figure 6 (right), it is depicted that for 298MHz the crossover point where dipoles outperform (B_1^+ ratio of dipole/loop) loop coils is around 6.2 cm in depth.

Although it is important to get the best B_1^+ efficiency possible, the comparison between different elements must be performed while taking SAR levels into account. The best element for optimal B_1^+ efficiency may differ from the best element for optimal $B_1^+/\sqrt{SAR_{max}}$ ratio. For a single element analysis if the best performing element for each depth is taken into consideration to plot $B_1^+/\sqrt{SAR_{max}}$ ratio over depth curves, the loop coil outperforms the dipole antenna. These results would lead to a conclusion that the dipole antenna is not the ideal element for deep imaging coil arrays but when paired together in arrays, the dipole antennas have inherently low coupling because of their smaller lateral extent and low Q-factor while in order to decouple several loop coils they need to be overlapped by a certain extent.

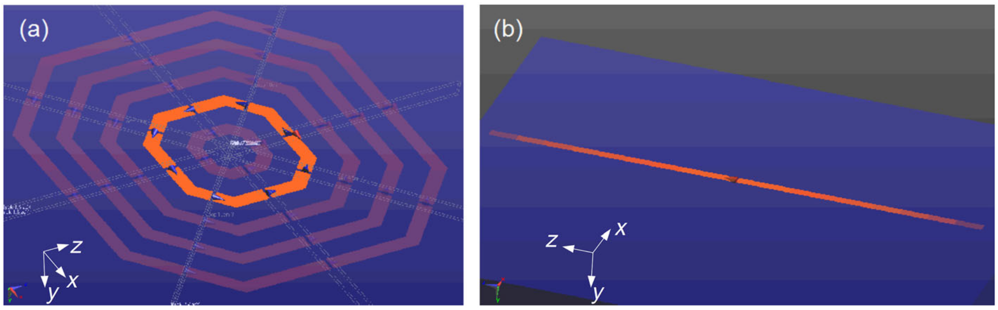

Figure 5: Simulation Geometries. B_0 field along z:(a) loop coil setup(all loop coils are shown; only one is active for each simulation);(b) dipole antenna setup [20].

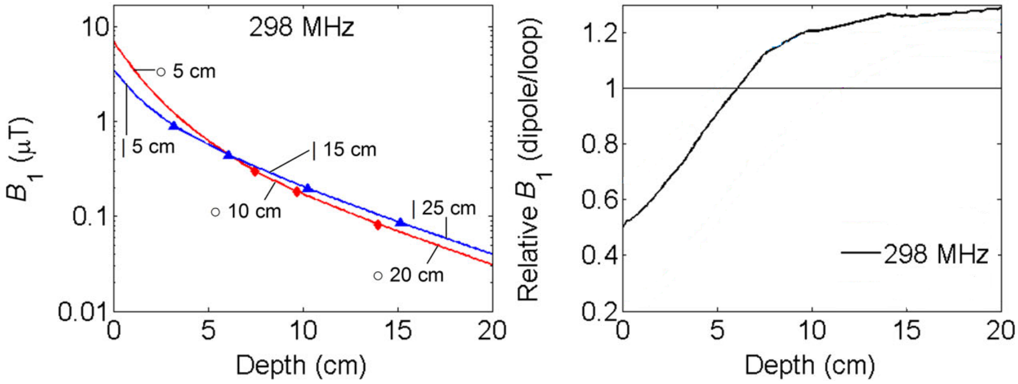

Figure 6: (left)B_1^+ profile along the maximum intensity projection over depth for the best performing element(red: loops; blue: dipoles) at 298MHz operating frequency; (right) B_1^+ ratio for dipole/loop over depth for 298MHz [20].

Dipole have their maximum SAR location directly underneath the center of the antenna, when displayed in an array, these maxima will not interact spatially with each other resulting in separated maximum SAR spots under each element. As for the loop coils, overlapping them in order to reduce inter-element coupling will cause high E-field regions to overlap potentially resulting in high (as high as four times) intensity SAR local levels.

To explore this effect, additional simulations were performed in this study by comparing an array of 3 loop coils overlapped for perfect decoupling with an array of 3 dipole antennas separated by the same center-to-center distance as the loop coil setup for 298MHz working frequency (Figure 7).

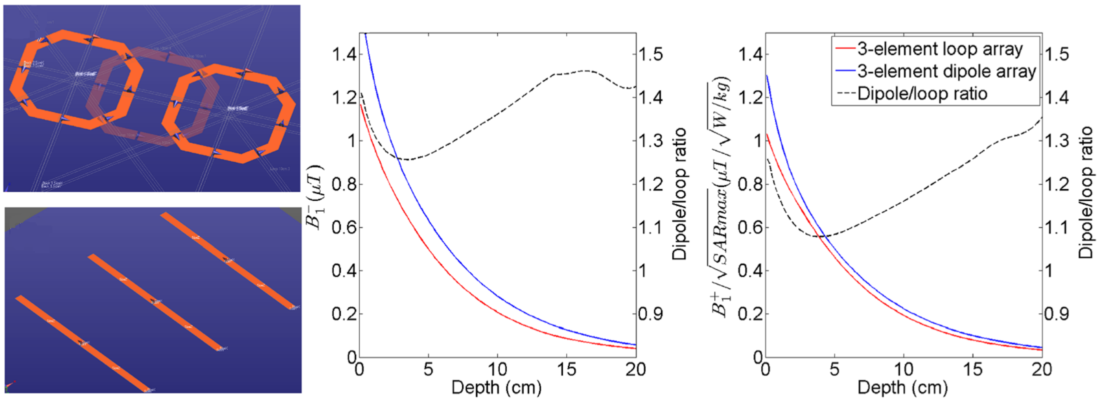

Figure 7: Simulation Geometries; B_1^+ profile at maximum projection and respective dipole/coil ratio; $B_1^+/\sqrt{SAR_{max}}$ profile at maximum projection and respective dipole/loop ratio [20].

Under these circumstances, the dipole antenna array has shown a 33% better efficiency and a 15% increase $B_1^+/\sqrt{SAR_{max}}$ ratio. These results show that for array operation the dipole elements outperform loop coils by a large margin countering what the single element analysis suggested.

2.5 Fractionated Dipole Antenna

As a successor of the SSAD antenna, the "fractionated dipole antenna" was introduced [21]. It consists of a 30-cm dipole antenna split into several segments all of which are connected by lumped elements in order to modify currents and voltages in the antenna to enhance performance. A study was made to compare the performance of this new antenna with the previously introduced SSAD antenna resulting in a decrease in SAR levels.

In order to clearly distinguish the effects of the lumped elements from the effects of the increase in dipole length, two separate studies were performed by numerical simulations. First, several dipole antennas without dielectric spacers were compared to the SSAD antenna performance in order to find the optimal length at a working frequency of 298MHz. Dipoles with lengths ranging from 5 to 45 cm with 5 cm increments were simulated using the software package SEMCAD X (Speag, Zurich, Switzerland) on a cubic phantom with a relative permittivity of 34 and a conductivity of 0.4 S/m. The resulting B_1^+ and local SAR distributions were used for the comparison with the SSAD antenna (Figure 8).

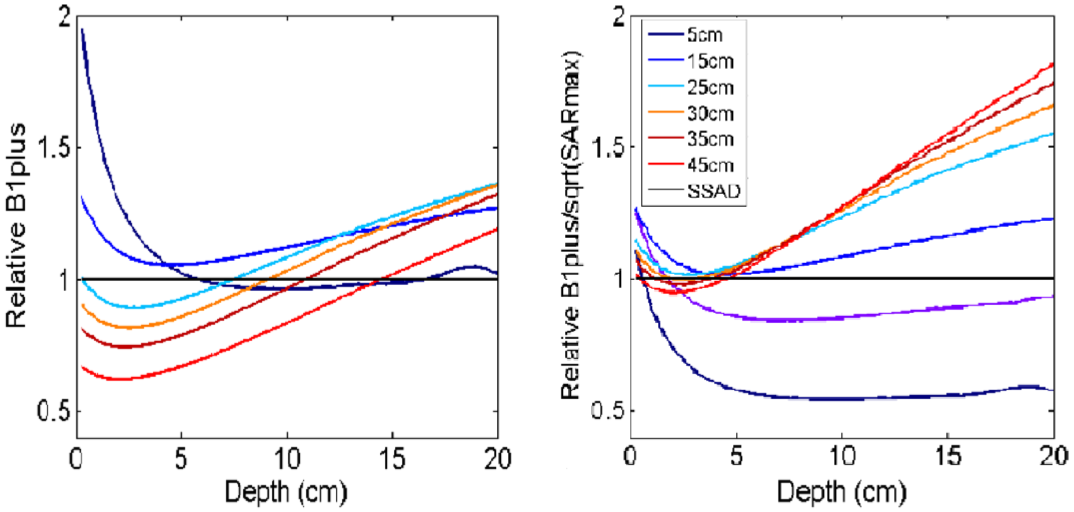

Figure 8: Simulation results of B_1^+ (left) and $B_1^+/\sqrt{SAR_{max}}$ (right) for a plain dipole antenna with varying length with the SSAD antenna as relative reference [21].

For deep body structures, at around 10 or 15 cm depth, the ideal dipole length was found to be between 30 and 40 cm.

Knowing this, to study the effects of segmenting the dipole with lumped elements, a length of 30cm was chosen because of its beneficial B_1^+ over $\sqrt{SAR_{max}}$ for a target depth of 10 cm which approximately corresponds to prostate depth. In this study, several lumped elements were tested in the fractionated dipole antenna and compared to the plain 30 cm in length dipole antenna under the same simulation conditions as the previous dipole vs. SSAD study.

The results from this simulation, depicted in Figure 9, clearly show that the use of intersegment capacitors provide a significant increase in B_1^+ strength for low depths ($<$10 cm) and no reduction for higher depths ($>$15 cm) while the use of intersegment inductors results in lower B_1^+ strength for all depths.

This would point towards concluding that using capacitors as intersegment elements would be the best choice, however, the decrease in SAR levels as a result of using inductors as intersegment elements largely outweighs the decrease in B_1^+ strength for lower depths resulting in a beneficial B_1^+ over $\sqrt{SAR_{max}}$ ratio. It can also be seen that the lowest effective SAR levels are achieved when using inductors of approximately 100 nH. Nonetheless, for higher inductor values, the performance steeply declines forcing the considered ideal value to be lowered to 75 nH for further antenna studies.

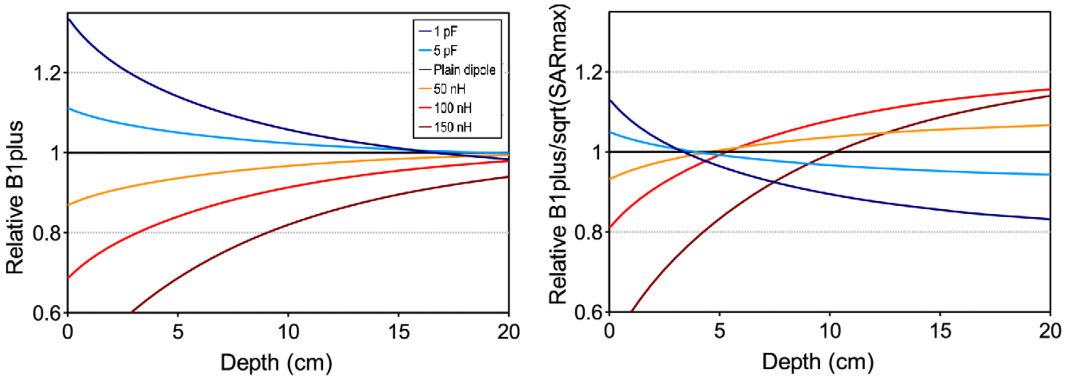

Figure 9: Simulation results of B_1^+ (left) and $B_1^+/\sqrt{SAR_{max}}$ (right) for a 30 cm fractionated dipole antenna with varying lumped element values with the 30 cm plain dipole antenna as relative reference [21].

After defining the ideal value for the lumped elements of the fractionated dipole antenna, two arrays, one of 8 fractionated dipole antennas and one of 8 SSAD antennas, were simulated on a human-like electromagnetic model in order to assess their performance on a prostate scan. To rate their performance, after the simulation, a phase-shim was applied to both arrays and the B1 field and SAR were recalculated with the ideal phase values for each channel.

In figure 10 we can see the simulation geometry (10a and d) as well as the receive performance (10b and e) and the $B1_1^+$ efficiency after phase-shimming (10c and f). It is clear that in terms of B_1^+ efficiency, both arrays are expected to perform in a similar way in the depicted region of interest (ROI, i.e. the prostate).

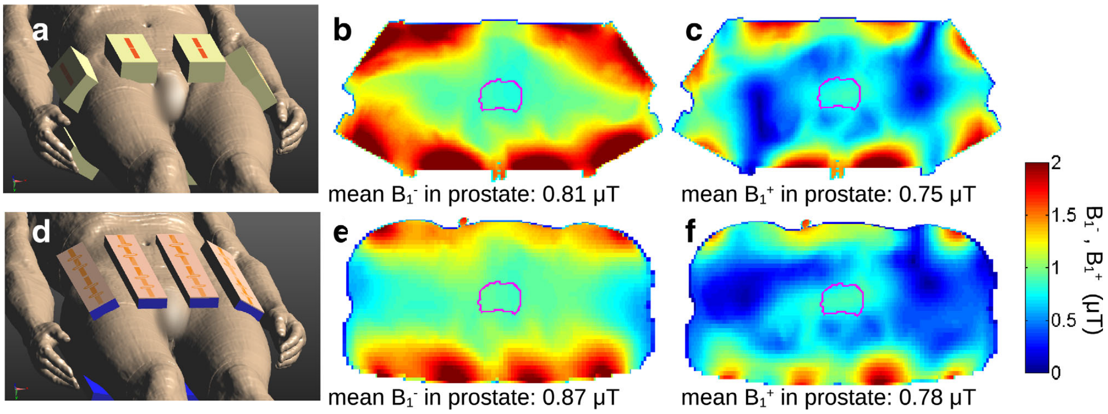

Figure 10: Simulation geometry (a and d), results of B_1^- receive performance (b and e) and B_1^+ efficiency after phase-shimming was applied (c and f) for both the SSAD antenna array (a,b,c) and the 30 cm fractionated dipole antenna array (d,e,f) [21].

For the same simulation setups, Figure 11a and c show the worst case scenario SAR distributions while Figures 11b and d show the SAR distributions for setups after phase-shimming was applied. The maximum SAR levels for each distribution are indicated below each figure. These results clearly depict much lower SAR levels for the fractionated dipole antenna array when compared to the SSAD antenna array.

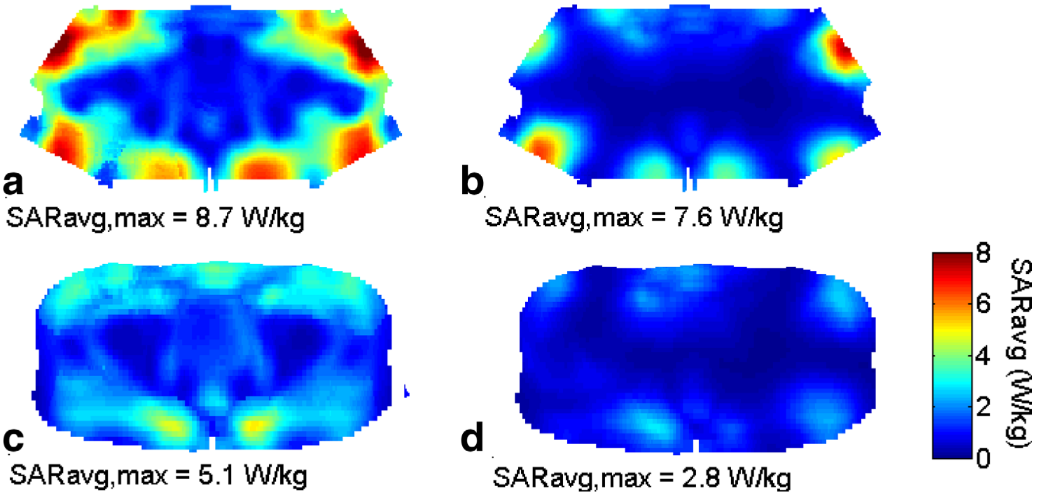

Figure 11: 10g Averaged Local SAR distributions and respective maxima: (a) Worst case scenario SAR for the SSAD antenna array; (b) SAR after phase-shimming for the SSAD antenna array; (c) Worst case scenario SAR for the fractionated dipole antenna array; (d) SAR after phase-shimming for the fractionated dipole antenna array [21].

To demonstrate the applicability of the newly suggested design, an 8 antenna array was built (Figure 12(left)) and used for prostate imaging (Figure 12(right)) on several volunteers to demonstrate the feasibility of prostate imaging with this setup. Currently, this experimental array is still used for prostate imaging purposes and many more, such as cardiac, kidney, liver, cervix cancer, axillary lymph nodes. Furthermore, the same antenna design is now incorporated in a breast coil and a head coil.

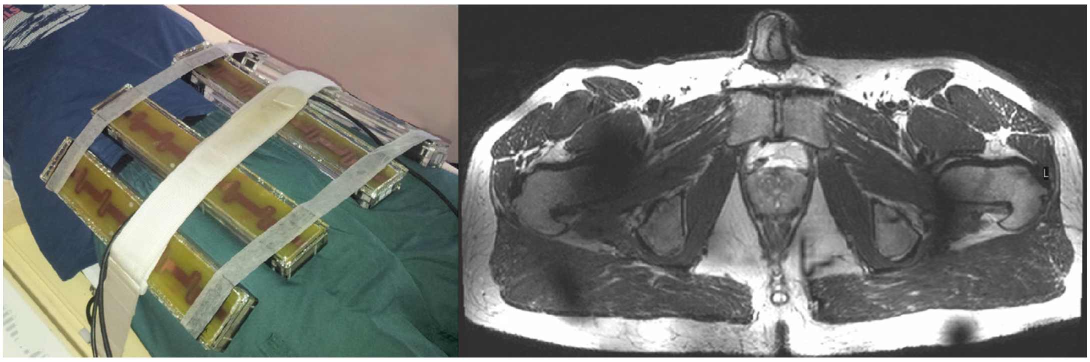

Figure 12: Fractionated Dipole antenna. (left) Elements with 20mm PMMA spacer and covers; (right)Correspondant T2w Turbo spin echo (TSE) healthy prostate imaging [21].

In conclusion, the fractionated dipole antenna takes the use of far-field antennas one step further but it presents itself as a difficult element to work with when aiming for massively parallel transmit due to the size needed to work efficiently. Nonetheless, it is also clear by analysing Figure 11 that the local SAR hotspots are always located underneath each array element pointing towards the hypothesis that a more continuous distribution of antennas around the pelvis might reduce effective SAR levels. This hypothesis supports the global aim of this project of creating a massively parallel transmit array.

2.6 Variations and Ongoing Research

Although recent publications do not seem to drift away susbtantially from the original dipole and loop antenna concepts, Winter *et al.* [22] introduced and built in 2013 a bow-tie-shaped antenna array and tested it for imaging and targeted RF heating purposes at 7T. This study had a lot of focus on the ability to induce targeted RF heating while also being applicable to imaging and therefore the conclusions do not directly translate to usable information regarding the aim of this project. Nonetheless, it is shown that this design of a far-field antenna is also applicable to MR imaging at high-field, namely 7T, and also a possible candidate for massively parallel transmit arrays if need be.

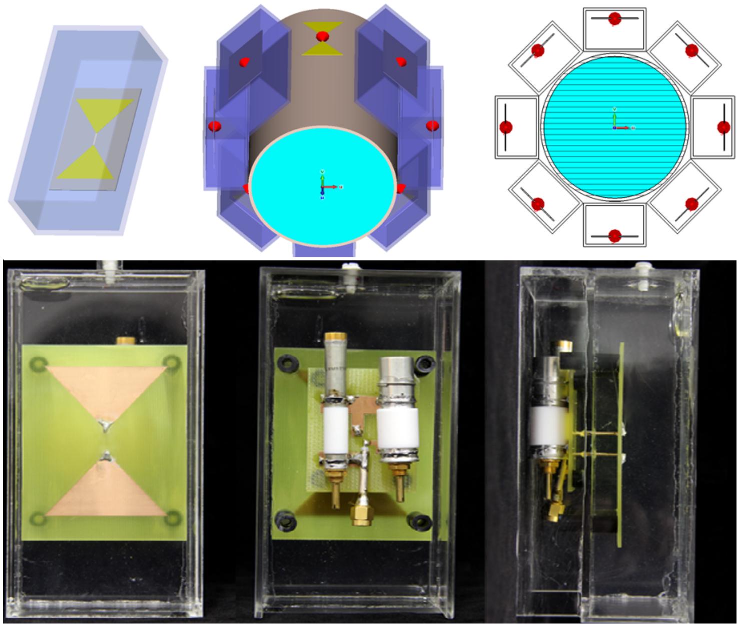

Figure 13: Bow-tie-antenna. (top) Simulation Geometry; (bottom) Built array element [22].

Although not always published, several other elements and combinations of different elements were tested as coil array elements and divulged to the community. Some examples of these studies are a prostate imaging study at 7T with transceive arrays [23], a deeper study on dipole antennas without dielectric substrates for head imaging [24][25], the combination of dipole antennas with loop coils working together in the same array [24][26][27] and the "folded dipole antenna" introduced by Lee *et al.* [28]. Furthermore, although kept as a last resort throughout this project, the bow-tie antenna alongside other less established elements, other commonly used antennas in other RF transmission dependant areas were not part of this investigation.

Simultaneously, there is constant ongoing research on new coil array element candidates at the Department of Radiology of the UMCU that if proven efficient can immediately be transferred into the proposed workframe.

2.7 Objective

As mentioned before, the analysis of SAR hotspots of already studied multichannel arrays lead to the global aim of testing out arrays with a higher count of channels and smaller elements, designated as massively parallel transmit arrays.

Having gathered information about the existent technology applicable to a massively parallel transmit array, the usage of this information was channelled into achieving the main objective to this project: consider existing and/or develop new RF antenna designs to use as different array elements in massively parallel transmit array geometries such that the B_1^+ field strength and transmit performance as well as potential SNR and receive performance is increased in a deeply located structure to be imaged, while at the same time maintaining SAR (Specific Absorption Rate) levels within the safety regulated values in order to minimize tissue heating due to deposited RF power.

3 Materials, Methods and Simulation Protocols

Given the broadness of the project this section will be split in three separate parts. These parts will be presented in logical and chronological order of the executed tasks. It begins with a description of the simulation-oriented developed work, followed by a detailed description of all the post-processing methods utilised to correctly draw conclusions from the simulation results and finally a brief explanation of the experimental part initiated after a solid result was obtained from the two previous subsections.

3.1 Simulation Environment

As mentioned before, the electromagnetic simulation environment Sim4Life (Zurich MedTech, Zurich, Switzerland) was used to study various potential massively parallel transmit array designs.

Each simulation can be divided into three major steps: geometry generation, simulation setup and analysys/data extraction. All of the the mentioned steps were performed with the help of Sim4Life's incorporated python scripting environment. All the geometries to be shown, were created in the scripting environment, and were simulated on a 120x250x400 mm^3 elipsoid phantom with ε_r=34 and σ=0.4 S/m to emulate human body behaviour. An example of a script and its corresponding generated geometry can be seen in Figure 14. All scripts used for this project will be included in Appendix B.

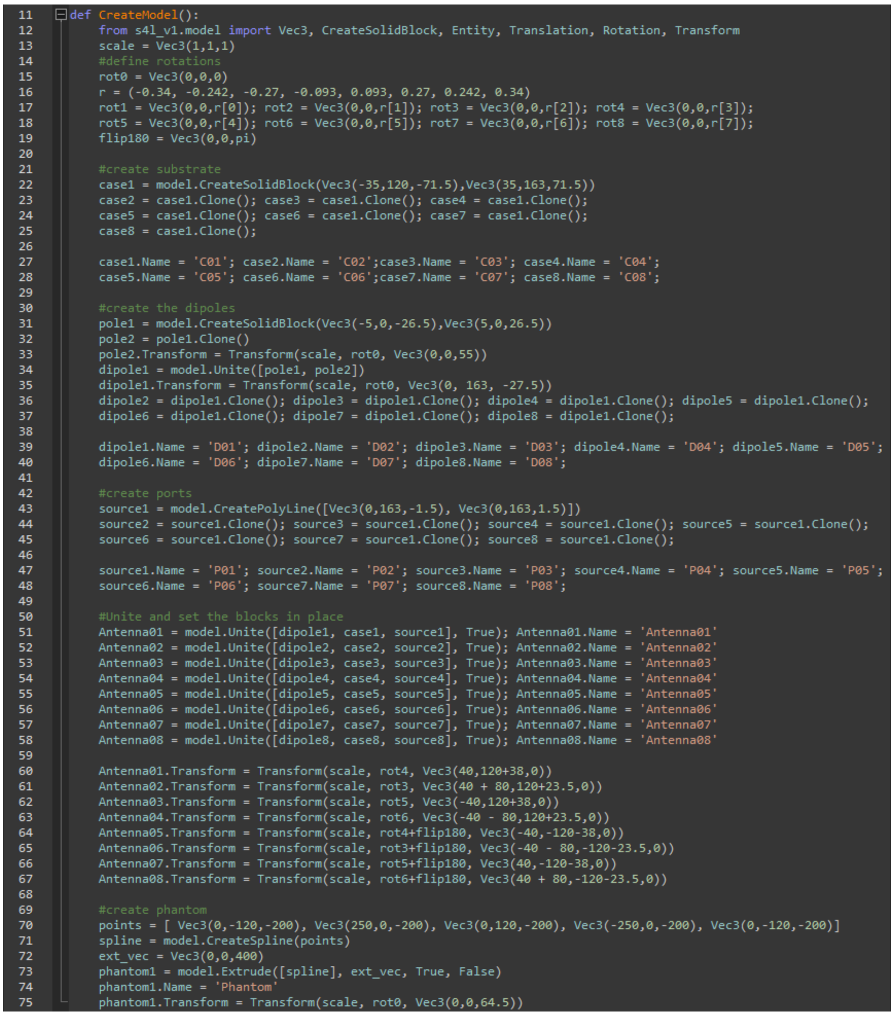

```python
def CreateModel():
    from s4l_v1.model import Vec3, CreateSolidBlock, Entity, Translation, Rotation, Transform
    scale = Vec3(1,1,1)
    #define rotations
    rot0 = Vec3(0,0,0)
    r = (-0.34, -0.242, -0.27, -0.093, 0.093, 0.27, 0.242, 0.34)
    rot1 = Vec3(0,0,r[0]); rot2 = Vec3(0,0,r[1]); rot3 = Vec3(0,0,r[2]); rot4 = Vec3(0,0,r[3]);
    rot5 = Vec3(0,0,r[4]); rot6 = Vec3(0,0,r[5]); rot7 = Vec3(0,0,r[6]); rot8 = Vec3(0,0,r[7]);
    flip180 = Vec3(0,0,pi)

    #create substrate
    case1 = model.CreateSolidBlock(Vec3(-35,120,-71.5),Vec3(35,163,71.5))
    case2 = case1.Clone(); case3 = case1.Clone(); case4 = case1.Clone();
    case5 = case1.Clone(); case6 = case1.Clone(); case7 = case1.Clone();
    case8 = case1.Clone();

    case1.Name = 'C01'; case2.Name = 'C02';case3.Name = 'C03'; case4.Name = 'C04';
    case5.Name = 'C05'; case6.Name = 'C06';case7.Name = 'C07'; case8.Name = 'C08';

    #create the dipoles
    pole1 = model.CreateSolidBlock(Vec3(-5,0,-26.5),Vec3(5,0,26.5))
    pole2 = pole1.Clone()
    pole2.Transform = Transform(scale, rot0, Vec3(0,0,55))
    dipole1 = model.Unite([pole1, pole2])
    dipole1.Transform = Transform(scale, rot0, Vec3(0, 163, -27.5))
    dipole2 = dipole1.Clone(); dipole3 = dipole1.Clone(); dipole4 = dipole1.Clone(); dipole5 = dipole1.Clone();
    dipole6 = dipole1.Clone(); dipole7 = dipole1.Clone(); dipole8 = dipole1.Clone();

    dipole1.Name = 'D01'; dipole2.Name = 'D02'; dipole3.Name = 'D03'; dipole4.Name = 'D04'; dipole5.Name = 'D05';
    dipole6.Name = 'D06'; dipole7.Name = 'D07'; dipole8.Name = 'D08';

    #create ports
    source1 = model.CreatePolyLine([Vec3(0,163,-1.5), Vec3(0,163,1.5)])
    source2 = source1.Clone(); source3 = source1.Clone(); source4 = source1.Clone(); source5 = source1.Clone();
    source6 = source1.Clone(); source7 = source1.Clone(); source8 = source1.Clone();

    source1.Name = 'P01'; source2.Name = 'P02'; source3.Name = 'P03'; source4.Name = 'P04'; source5.Name = 'P05';
    source6.Name = 'P06'; source7.Name = 'P07'; source8.Name = 'P08';

    #Unite and set the blocks in place
    Antenna01 = model.Unite([dipole1, case1, source1], True); Antenna01.Name = 'Antenna01'
    Antenna02 = model.Unite([dipole2, case2, source2], True); Antenna02.Name = 'Antenna02'
    Antenna03 = model.Unite([dipole3, case3, source3], True); Antenna03.Name = 'Antenna03'
    Antenna04 = model.Unite([dipole4, case4, source4], True); Antenna04.Name = 'Antenna04'
    Antenna05 = model.Unite([dipole5, case5, source5], True); Antenna05.Name = 'Antenna05'
    Antenna06 = model.Unite([dipole6, case6, source6], True); Antenna06.Name = 'Antenna06'
    Antenna07 = model.Unite([dipole7, case7, source7], True); Antenna07.Name = 'Antenna07'
    Antenna08 = model.Unite([dipole8, case8, source8], True); Antenna08.Name = 'Antenna08'

    Antenna01.Transform = Transform(scale, rot4, Vec3(40,120+38,0))
    Antenna02.Transform = Transform(scale, rot3, Vec3(40 + 80,120+23.5,0))
    Antenna03.Transform = Transform(scale, rot5, Vec3(-40,120+38,0))
    Antenna04.Transform = Transform(scale, rot6, Vec3(-40 - 80,120+23.5,0))
    Antenna05.Transform = Transform(scale, rot4+flip180, Vec3(-40,-120-38,0))
    Antenna06.Transform = Transform(scale, rot3+flip180, Vec3(-40 - 80,-120-23.5,0))
    Antenna07.Transform = Transform(scale, rot5+flip180, Vec3(40,-120-38,0))
    Antenna08.Transform = Transform(scale, rot6+flip180, Vec3(40 + 80,-120-23.5,0))

    #create phantom
    points = [ Vec3(0,-120,-200), Vec3(250,0,-200), Vec3(0,120,-200), Vec3(-250,0,-200), Vec3(0,-120,-200)]
    spline = model.CreateSpline(points)
    ext_vec = Vec3(0,0,400)
    phantom1 = model.Extrude([spline], ext_vec, True, False)
    phantom1.Name = 'Phantom'
    phantom1.Transform = Transform(scale, rot0, Vec3(0,0,64.5))
```

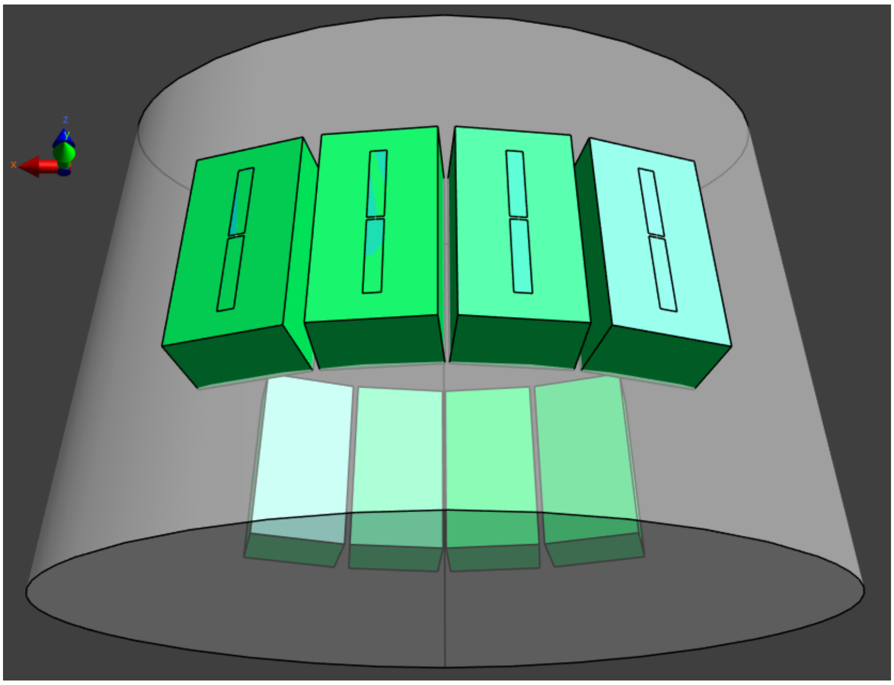

Figure 14: Example geometry generator python script and corresponding output

The three basic antenna designs from which all the simulated arrays were derived from are shown in Figure 15. All the three designs were thoroughly investigated and compared in terms of performance in order to find the ideal candidate for a massively marallel transmit array.

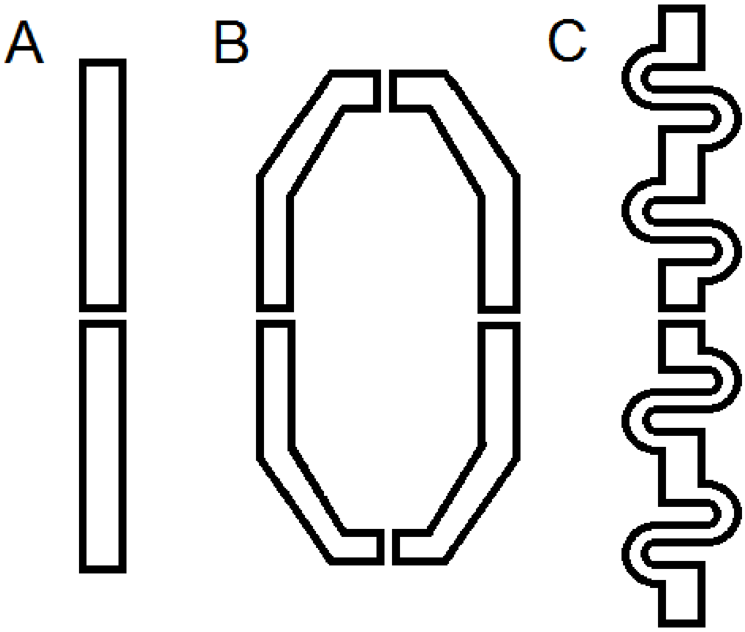

Figure 15: The three basic antenna shapes: the starting point of the massively parallel transmit array. A) Dipole Antenna; B) Loop Antenna; C) Fractionated Dipole Antenna.

The first antenna shape undergoing investigation was the Dipole Antenna (Figure 15A). Starting from an already existent design (the SSAD antenna, section 2.2) the dipole was miniaturized, had its placement altered and substrate changed, to corroborate that good results could be obtained without any substrate as mentioned in section 2.2. These changes were implemented in several combinations in order to find the best performing array composed of miniaturized dipoles. In Figure 16 both the starting and the final point of the dipole miniaturizing process are shown while an explanation regarding the other variations will be briefly discussed in Appendix A.

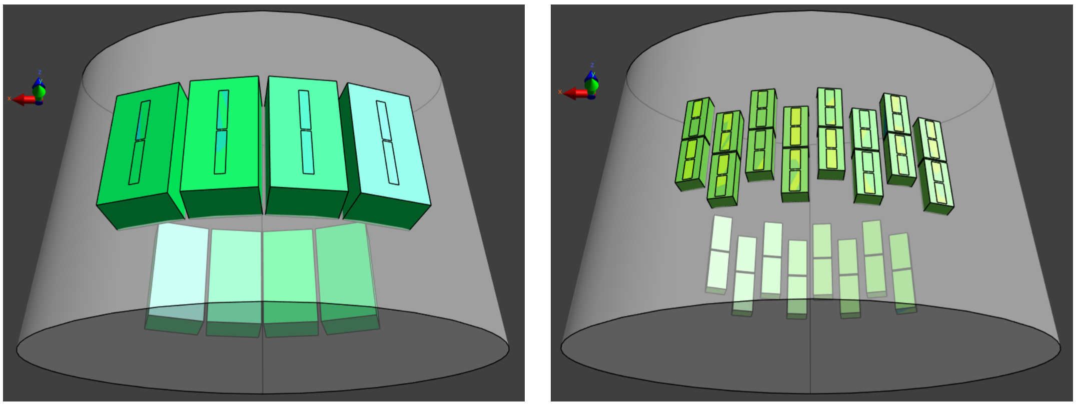

Figure 16: Comparison between the starting point of the geometry investigation, the 8-channel SSAD antenna array (left), and the final result of a thorough material, size and spacial position analysis of the new miniaturized dipole, the 32-channel Intercalated Short Dipole antenna array (right).

Having obtained satisfying results with the dipole antenna, the next basic antenna shape, the loop antenna, was then re-designed as a small element (Figure 19). In order to achieve the best possible 32-channel Loop array, several steps had to be taken. First the loop as a single element had to be matched to 50 Ω by iteratively replacing the capacitors placed on each side of the loop (4 in total) until the frequency response showed resonance at the required frequency (298 MHz). Furthermore, having the capacitors tuned to match the 50 Ω current at the working frequency of 298MHz, as loops tend to be a geometry highly sensitive to coupling between elements, precautions had to be taken in order to minimize the power lost through this coupling effect. This was obtained by overlapping the immediate neighbouring elements (which are more prone to coupling) as described in section 1.9 and visible in Figure 17a).

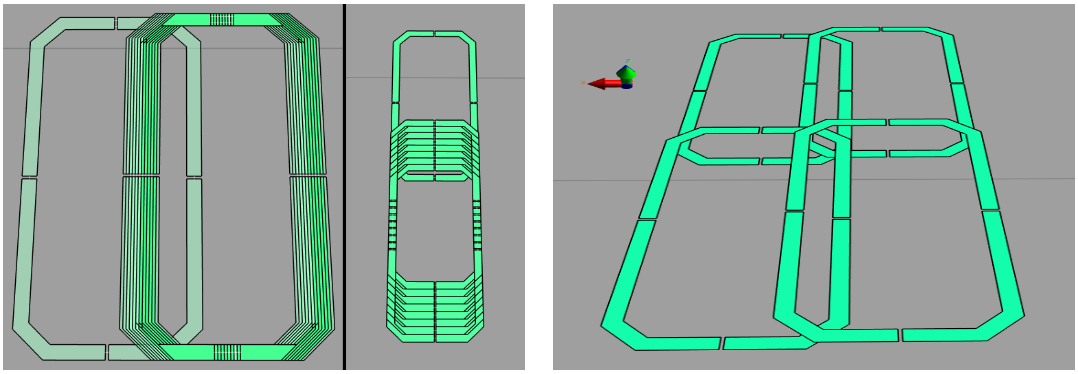

(a) Atempts to find the ideal overlap (b) 4 individual loops overlapped ideally

Figure 17: Procedure used to find the ideal overlap that minimizes inter-element coupling.

Although it is hard to obtain ideal decoupling for a 4-loop setup as depicted in Figure 17b), when scaling the setup to a larger number of channels and consequentially a higher number of elements, new problems arise due to nearest neighbour coupling not being the only significant coupling. Loops and their characteristic high inter-element coupling make the next nearest neighbours also have significant coupling. To test if the decoupling efficiency of the overlap still applied to an array with a larger number of elements, the 4 loops setup was replicated to both sides keeping the ideal overlap between nearest neighbours in order to check if said array with a 12-channel count would still be somewhat acceptably decoupled. For this, the S-Parameters for the 12 loops were checked to see if the decoupling we sought was obtained. In Figure 18 the S-Parameter matrix for all the 12 elements is shown.

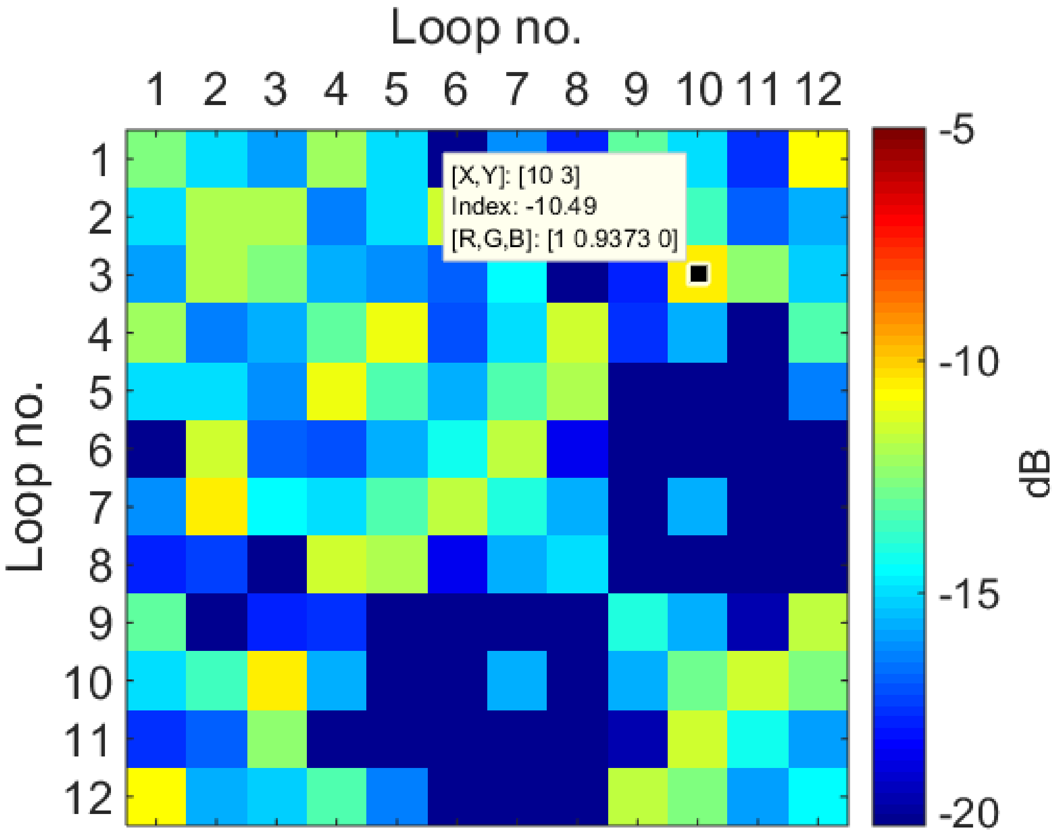

Figure 18: Graphic depiction of the S-Parameter matrix, at 298MHz of a 12-channel ideally overlapped loop array where the maximum S-Parameter is of -10.49 dB, corresponding to a loss of power due to coupling of approximately 10%.

The resulting decoupling was not ideal, although acceptable, since no element lost much more than 10% power due to coupling.

After obtaining the best possible matching, tuning and decoupling of the elements, an array consisting of 32 individual elements was generated and spatially distributed according to the best decoupling scenario obtained. The resulting array can be seen in Figure 19 alongside with the correspondent S-Parameter matrix.

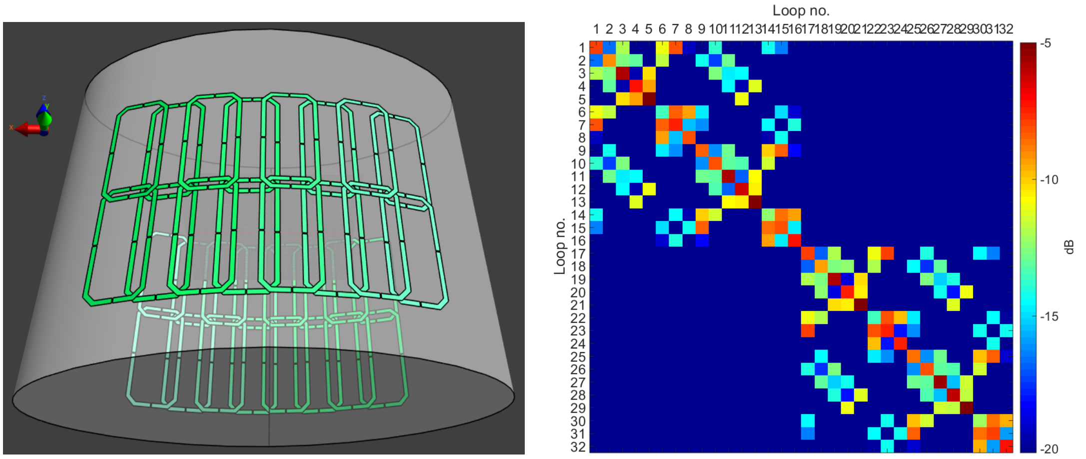

(a) 32-channel loop array (b) S-Parameter matrix at 298MHz

Figure 19: a) Resulting spatial distribution of the small loop antennas in a 32-channel array after obtaining the best matching, tuning and decoupling of the elements alongside with b) the graphic depiction of the S-Parameter matrix of a 12-channel ideally overlapped loop array.

As we can see in Figure 19b) the overlap decoupling when applied to a 32-channel loop array that was bent to fit the curvature of an ellipsoid phantom still yields acceptable results for most of the inter-element coupling (only 4 entries above -10dB). As for the self coupling (diagonal of the matrix), the non-linear load throughout the phantom (each loop "sees" the phantom from a different position) causes the elements to be mismatched with the 50Ω again leading to a stronger power reflection back to the current source. This issue with self-coupling will not be a problem because all simulation results will be normalized to accepted power to virtually cancel this effect.

It is important to state that coupling was only considered and sought to be minimized when working with the loop antennas due to it being a geometry prone to high coupling between elements. Both the dipoles and the fractionated dipoles were assumed to have ideal minimal coupling.

Concluding the investigation referent to the loop antenna, the next step was initiated focusing on the fractionated dipole antenna which was a promising design for the massively parallel transmit array as discussed in section 2.5.

For the fractionated dipole, as it was for the regular dipole, several tries were undertaken in the search for the best performing array. In Figure 20 we can see all the simulated geometries used in the final analysis process in section 4 when the aim was reaching a 32-channel system. In this figure, we can see that a first attempt consisted in spatially compressing the distribution of the already existent fractionated dipoles in order to fit 16 dipoles in the same space as 8 would normally be placed. This was achievable by intercalating the fractionated dipoles similarly to what had been done with the regular dipoles.

As a second variation, the fractionated dipole was split in half and driven on the edge turning into a 32-channel array in which each element consisted of a long leg, attached to a small conductive patch where the element was driven, due to this element only having one long leg, it was considered a "fractionated monopole".

The third and final variation, the half-size fractionated dipole antenna, was obtained by once again splitting the dipole in half, obtaining two half-size dipoles and driving each of the smaller dipoles in their center, completing the 32-channel requisite.

One more geometry was simulated but no change was done to the shape of the half-size fractionated dipole elements. Only a placement rearrangement was done to reduce SAR values for this array, as it will be explained in 4.

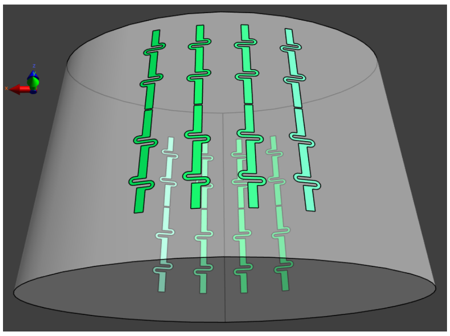

(a) 8-channel fractionated dipole antenna array

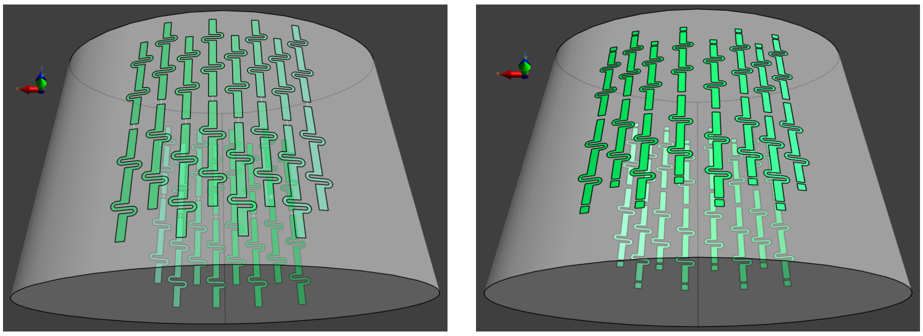

(b) 16-channel fractionated dipole antenna array

(c) 32-channel fractionated monopole antenna array

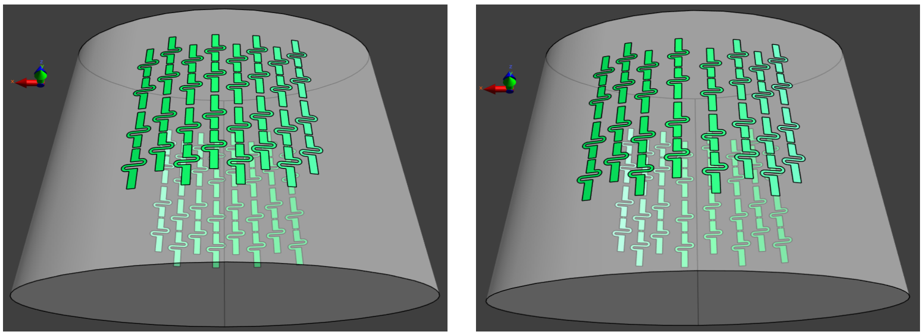

(d) 32-channel half-size fractionated dipole antenna array

(e) 32-channel half-size fractionated dipole antenna array (non-linear spacing)

Figure 20: Comparison between the starting point of the geometry investigation regarding the fractionated dipole antenna as steps of a thorough size and spatial position analysis of the fractionated dipole.

Before concluding the geometry generations, three more setups were generated. These three 24-channel setups were generated not to actively seek a better performing array but as a preparation step for building the ideal array since currently, hardware constraints, only allowed us to drive a maximum of 24-channels simultaneously at the 7 Tesla scanner used for testing. These constraints will be further discussed in section 4. In Figure 21 these three last setups can be seen as generated by Sim4Life. Two of these setups were tested on the previously used phantom while the best performing of the two was then simulated on a realistic human model, named Duke.

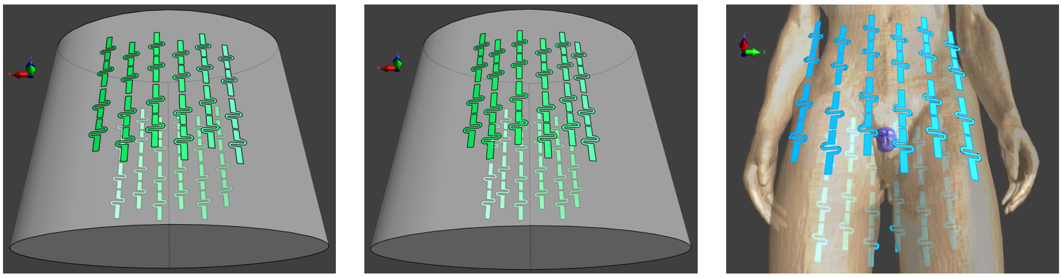
(a) 24-channel half-size fractionated dipole antenna array on a phantom

(b) 24-channel half-size fractionated dipole antenna array (non-linear spacing) on a phantom

(c) 24-channel half-size fractionated dipole antenna array on DUKE

Figure 21: Geometries generated as proof of concept to later build a 24-channel array compatible with the hardware requirements of the 7 Tesla scanner.

The next step taken after geometry generation was the simulation setup. This entire process was also performed relying on the python scripting environment and were set to be concordant with the default settings of Sim4Life. Before running each simulation, an important step has been taken, the connectivity of the voxelization of each model was thoroughly checked in order to ensure the trustworthiness of the output results. Once the simulations had been completed, extraction of the output data was also performed relying on python scripting where the Transmit Field ($\mathbf{B}_1$), Current Density ($\mathbf{J}$) and Electric Field ($\mathbf{E}$) were directly saved as MATLAB (The Mathworks, Inc., Natick, Massachusetts, United States) files. All the scripts used to extract this data will also be included in Appendix B.

3.2 Post-processing

The first post-processing step performed on the extracted data was the B_1^+ shimming. The method explained on section 1.5 was implented in MATLAB with the intent of maximizing the B_1^+ intensity on a given ROI inside the phantom. For this, a 3cm radius spherical mask was created in the center of the phantom directly underneath the simulated array. This mask was then used as the B_1^+ shimming ROI. For the simulation on the human model Duke, the chosen ROI was a 3cm radius spherical mask centred on the centre of Duke's prostate.

The B_1^+ shimming optimization problem was solved using the pattern search method available in MATLAB's libraries. Given the complexity of the problem derived from the amount of driving channels simulated, the solution finding script was iterated 200 times with different starting points in order to minimize the chances of finding a solution that is actually a local minimum. As an example in Figure 22 we can see the result of the B_1^+ shimming method on data of an 8-channel SSAD array setup.

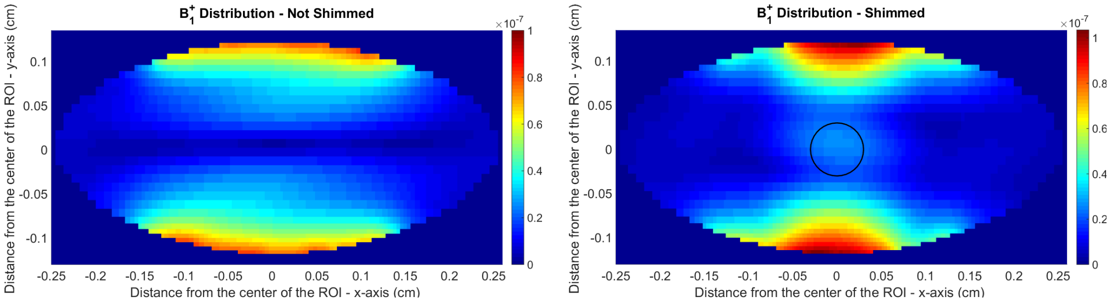

Figure 22: Difference between B_1^+ (T) distribution of a 8-channel SSAD setup before and after shimming was performed over the depicted region (black circle).

Having identified the shim settings that would result in the best outcome the settings were then transferred back to Sim4Life as an input to calculate the 10 gram averaged SAR, as described in section 1.6.

Additionally, Sim4Life's scripting environment was used to calculate the potential SNR for each of the arrays following the method described in section 1.8.

Apart from these three major post-processing steps, only minor calculations were performed with the extracted data in order to obtain quantities suited for an easy comparison of all the simulated quantities. Namely, obtaining relevant ratios between extracted quantities over the entire simulated area or averaging meaningful quantities over the shimmed ROI.

Once again, all scripts relevant to this section can be found in Appendix B.

3.3 Experimental Phase

The last step of this project was building the best performing array (simulation wise) that was compatible with hardware constraints already mentioned (24-channel maximum transmit channels). For this, 24 half-size fractionated dipole antennas were delivered as requested on a printed circuit board (PCB). A single element can be seen in Figure 23 before any matching work was done to it.

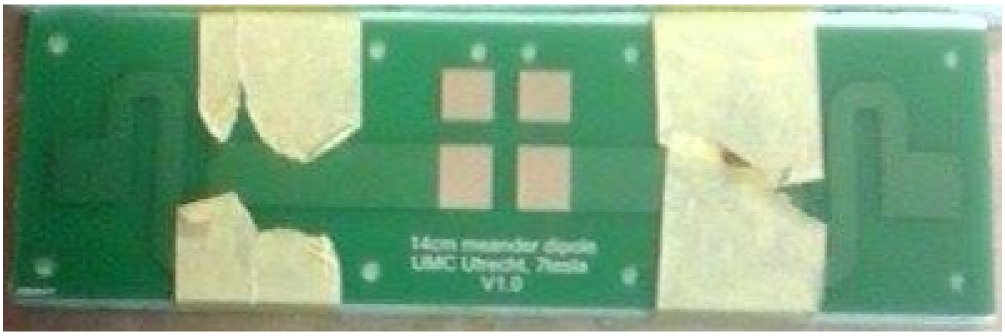

Figure 23: Half-size fractionated dipole antenna mounted on a 10mm thickness foam plate to mimic the 10mm distance the antenna was placed from the body in all simulations.

From section 2 we can recall that the ideal length for a dipole to be naturally matched to 50Ω was around 30cm. Knowing that our half-size element (14cm in length) is more than half said ideal length, it was expected to be a hard task to match it correctly.

For matching of all elements a network analyser was used calibrated to 50Ω at the working frequency of 298MHz in order to achieve an acceptable matching by adding lumped elements to our pre-antenna circuitry. The software used to find what lumped elements were necessary to match the antennas was PASAN (Free Software Foundation Inc., Boston, Massachusetts, EUA). In Figure 24, a PASAN screen capture, we can see the on a Smith Chart (a visual tool to easily track impedance changed) the starting point (the original impedance of the antenna) of around 24.7 - 229jΩ as well as the desired matching and the path taken, by iteratively changing the type and value of the lumped element (left of the figure), to reach it.

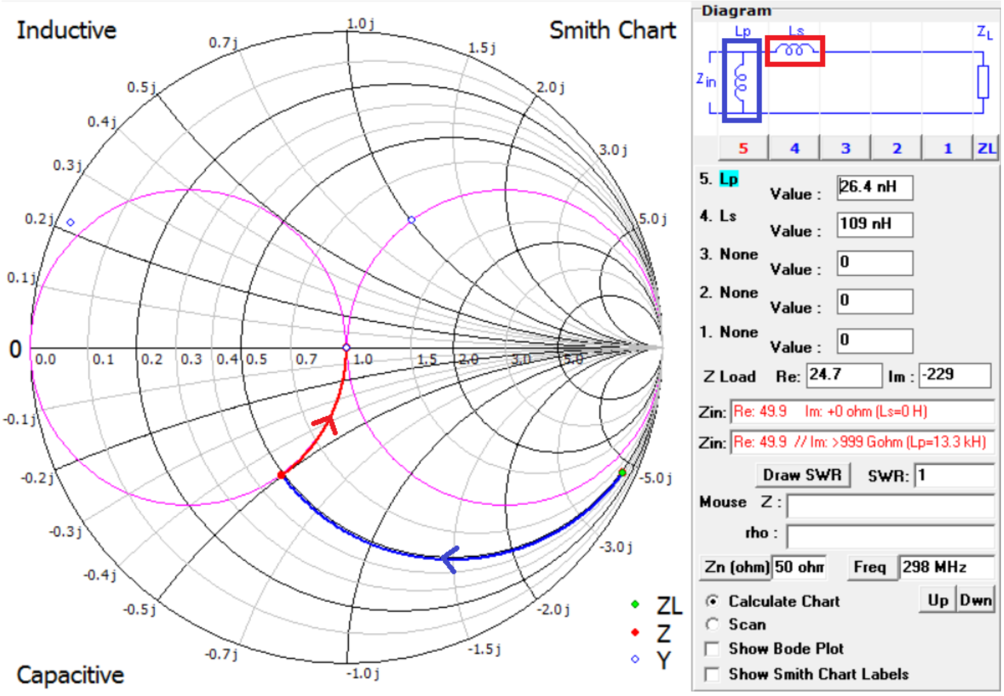

5. Lp Value : 26.4 nH

4. Ls Value : 109 nH

3. None Value : 0

2. None Value : 0

1. None Value : 0

Z Load Re: 24.7 Im : -229

Zin: Re: 49.9 Im: +0 ohm (Ls=0 H)

Zin: Re: 49.9 // Im: >999 Gohm (Lp=13.3 kH)

SWR: 1

Mouse Z :

rho :

Zn (ohm) 50 ohm Freq 298 MHz

● Calculate Chart

○ Scan

☐ Show Bode Plot

☐ Show Smith Chart Labels

Figure 24: Screen capture of PASAN depicting the matching process necessary to apply to each antenna if all components were ideal.

Now knowing that two inductors, one in parallel and one in series, would be needed and that no inductors available for use in the UMCU antenna lab had such a high inductance value, the inductors had to be manually built as a series of loops of conductive wire. Also, no real components are 100% trustworthy, that is, parasitic inductance/resistance is present let alone a self-built inductor. This lead to an extensive iterative process to try and find what inductors lead to a good matching of the antennas which seemed to vary with each antenna and with each inductor built. This matching was, as mentioned, sought after using a network analyser, and all antennas where tweaked until the matching was close to ideal as seen in Figure 25. In this Figure, we can see the natural impedance (yellow line) of the antenna being matched in the center of the smith chart (already at 50Ω) and the power reflection (green line) at -49.788 dB at the resonant frequency of 298MHz.

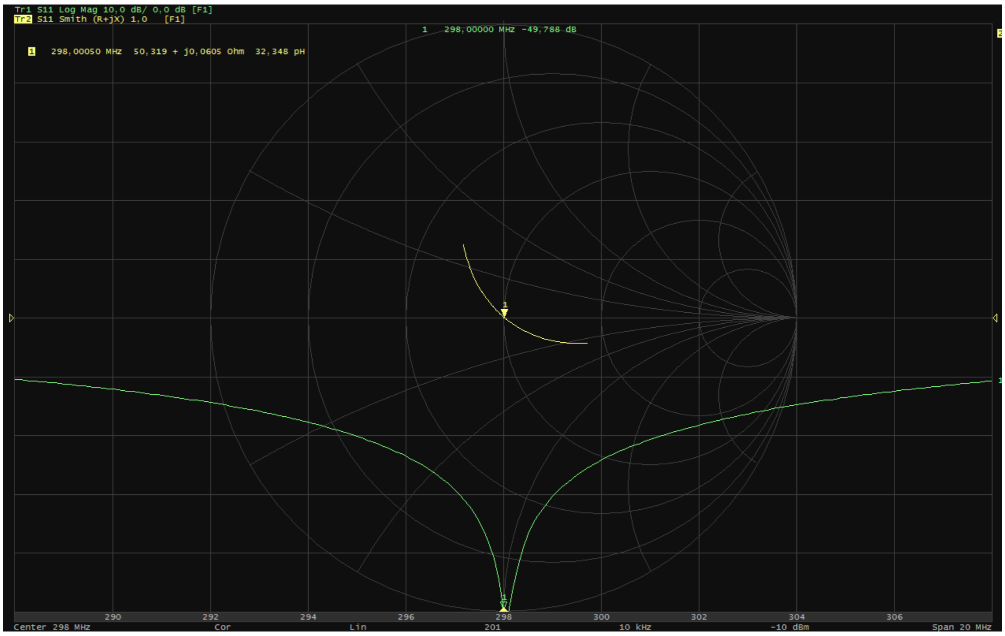

```
Tr1 S11 Log Mag 10,0 dB/ 0,0 dB [F1]
Tr2 S11 Smith (R+jX) 1,0   [F1]
1   298,00000 MHz -49,788 dB
1   298,00050 MHz  50,319 + j0,0605 Ohm  32,348 pH
Center 298 MHz   Cor   Lin   201   10 kHz   -10 dBm   Span 20 MHz
```

Figure 25: Screen capture of the network analyser interface showing the response of a ideally matched half-size fractionated dipole antenna.

Finally all 24 elements were matched using this iterative method and the final result can be seen in Figure 26.

Figure 26: Half-size fractioned dipole antennas matched to 50Ω with the addition of two inductors.

After having all the 24 antennas correctly matched, all cables were attached to the antennas and the process of building the array started. As done in the simulations, a top and bottom arrays were created in an intercalated disposition as seen in Figure 27 and set it up with a 10mm foam spacer on an octagonal, pelvis shaped, phantom filled with ethylene glycol with 35 g/l salt and air tubes inside as used in [21]. As seen in Figure 28 the phantom has a filling chimney which renders impossible the placement of one of the elements which lead us to drive the array with 23 channels instead of the original idea of 24.

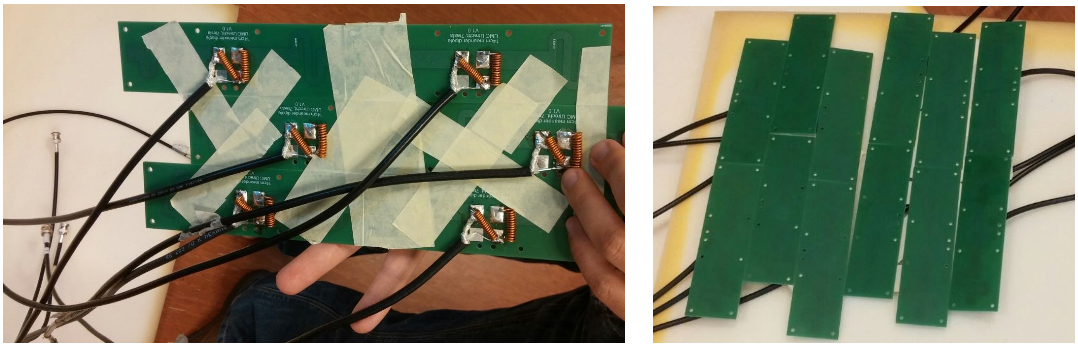

(a) Half of the top array

(b) Bottom array

Figure 27: The half-size fractionated dipole antennas where put together in an intercalated fashion, divided into a top and a bottom array, to mimic the simulation scenarios as faithfully as possible.

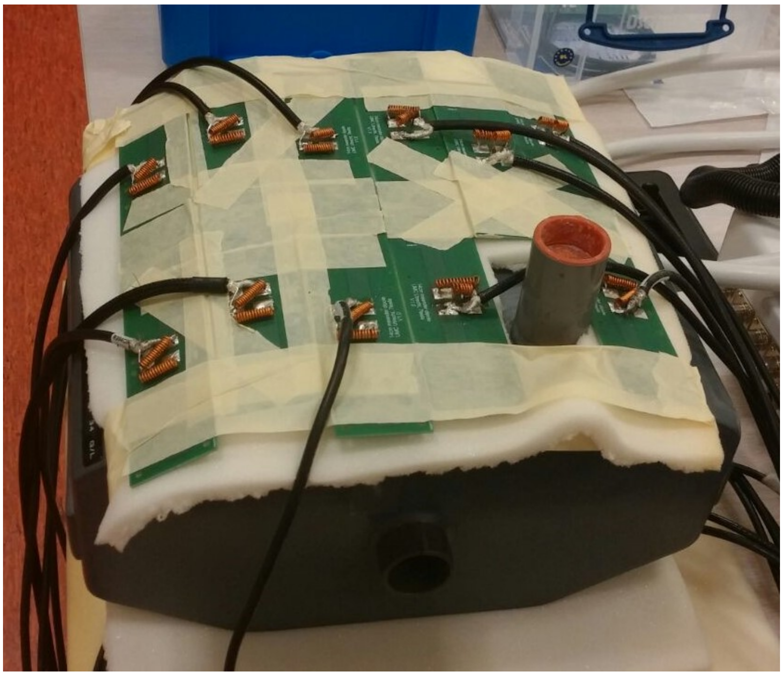

Figure 28: 23-channel half-size fractionated dipole antenna array on salt-water phantom. Notice the filling chimney that prevents the array from having the 24th element connected.

Finally, the array was connected to the scanner and tested. The tests performed were fairly simple since the aim was not to prove that the array is ready for MR implementation but to check if the array was functional. For this a quick survey scan was performed to check if the receive regime of the array was working and for the transmit, a DREAM [29] scan was performed to construct a B_1^+ map.

4 Results and Discussion

As stated before, all geometries were built with the Sim4Life Python Scripter and all simulations were performed using the Sim4Life FDTD package. A collection of the most meaningful results will be presented in this chapter divided into a stepwise selection of the best performing array as follows:

Step A. Comparing the basic antenna shapes;

Step B. Comparing different morphologies derived from the best performing shape of Step A;

Step C. Comparing different placements of the best performing morphology of Step B.

Each step will comprise of a display of the most relevant factors for transmit and receive efficiency analyzed while comparing the several geometries. The transmit performance will mainly be evaluated in terms of the $B_1^+/\sqrt{pSAR10g}$ ratio and the receive performance by the SNR values.

4.1 Step A: Finding the best antenna shape

The logical step to start the investigation was to compare the basic antenna shapes covered in section 2 using the framework described in detail in section 3. In Figures 30 through 34 we can see the visual interpretation of the B_1^+, $B_1^+/\sqrt{pSAR10g}$, Averaged 10g SAR and SNR distributions of the original 8-channel SSAD array, the best performing 32-channel miniaturized dipole array, a 32-channel small loop array and the original 8-channel fractionated dipole antenna array. All these geometries can be seen in Figure 29.

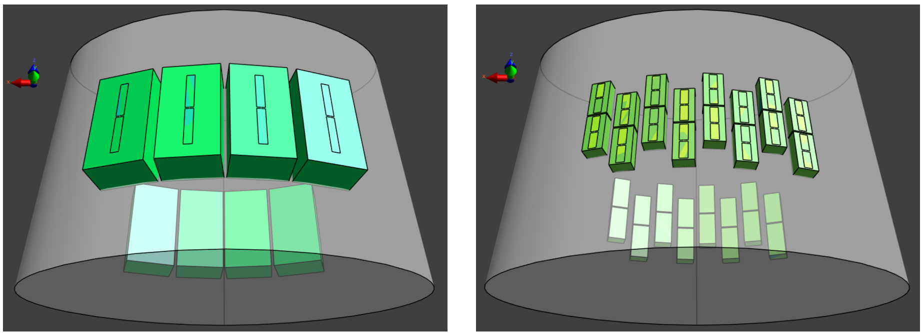

(a) 8-channel SSAD antenna array

(b) 32-channel intercalated miniaturized dipole antenna array

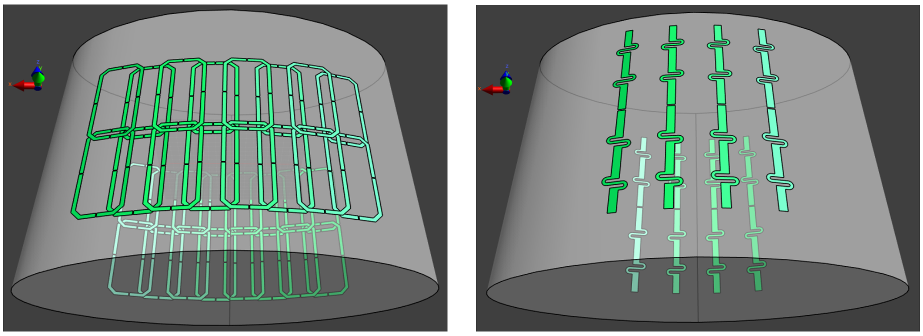

(c) 32-channel minaturized loop antenna array

(d) 8-channel fractionated dipole antenna array

Figure 29: Sim4Life's python scripting generated geometries studied in Step A.

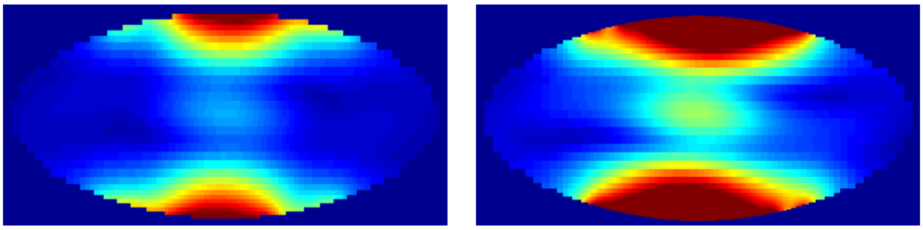

(a) 8-channel SSAD antenna array

(b) 32-channel intercalated miniaturized dipole antenna array

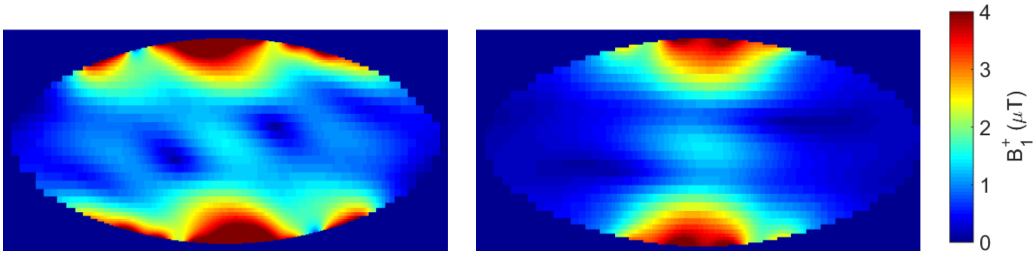

(c) 32-channel minaturized loop antenna array

(d) 8-channel fractionated dipole antenna array

Figure 30: B_1^+ distributions optimally shimmed through a 3cm radius sphere at the center of the phantom directly beneath the array (same ROI as in Figure 22) for the array designs studied in Step A. All distributions have been normalized to 32W accepted power per array.

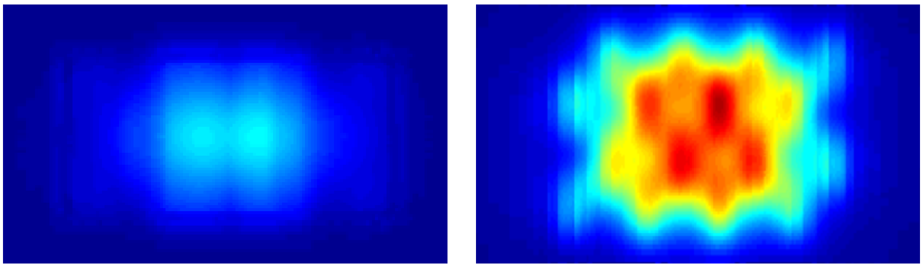

(a) 8-channel SSAD antenna array

(b) 32-channel intercalated miniaturized dipole antenna array

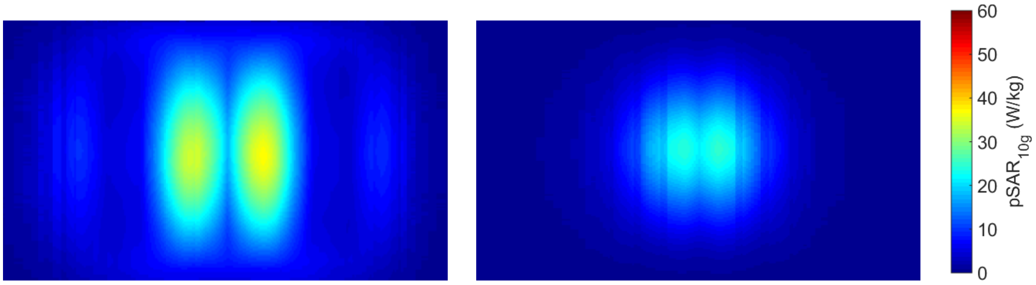

(c) 32-channel minaturized loop antenna array

(d) 8-channel fractionated dipole antenna array

Figure 31: Coronal maximum intensity projection of the Peak 10g Averaged SAR (pSAR10g) resultant from optimally shimming through a 3cm radius sphere at the center of the phantom directly beneath the array (same ROI as in Figure 22) for each of the array designs studied in Step A.

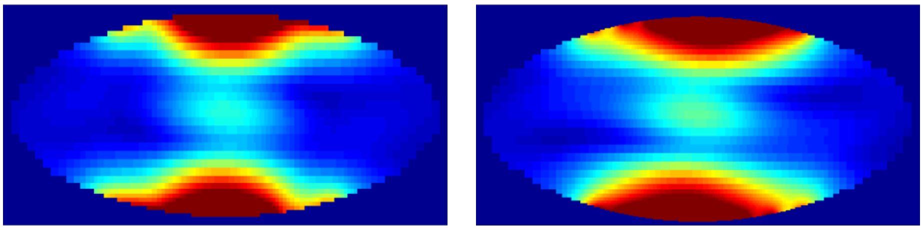

(a) 8-channel SSAD antenna array

(b) 32-channel intercalated miniaturized dipole antenna array

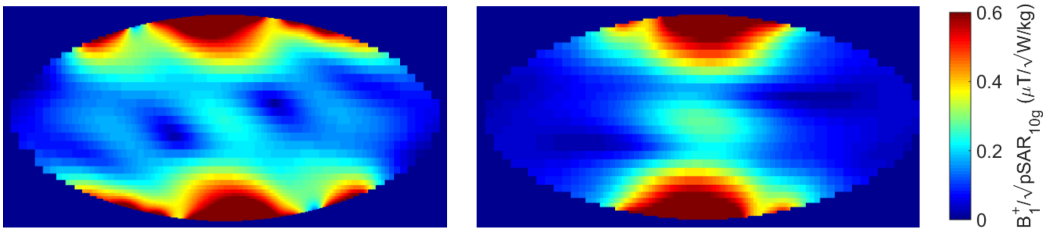

(c) 32-channel minaturized loop antenna array

(d) 8-channel fractionated dipole antenna array

Figure 32: B$_1^+$ over $\sqrt{pSAR10g}$ ratio distributions optimally shimmed through a 3cm radius sphere at the center of the phantom directly beneath the array (same ROI as in Figure 22) for each of the array designs studied in Step A.

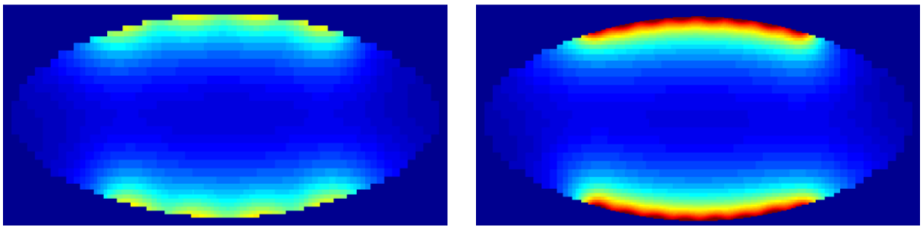

(a) 8-channel SSAD antenna array

(b) 32-channel intercalated miniaturized dipole antenna array

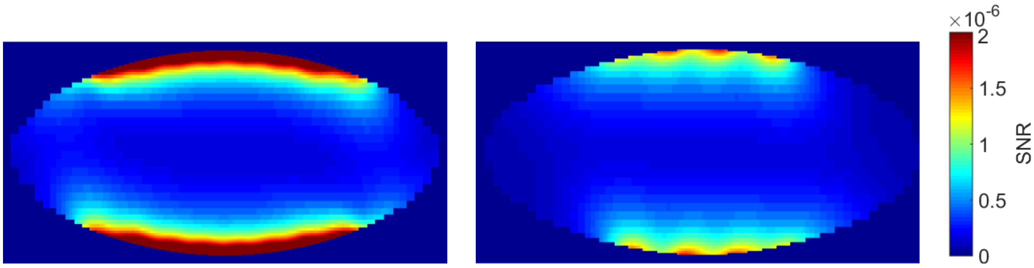

(c) 32-channel minaturized loop antenna array

(d) 8-channel fractionated dipole antenna array

Figure 33: Potential SNR values for each voxel for each of the array designs studied in Step A.

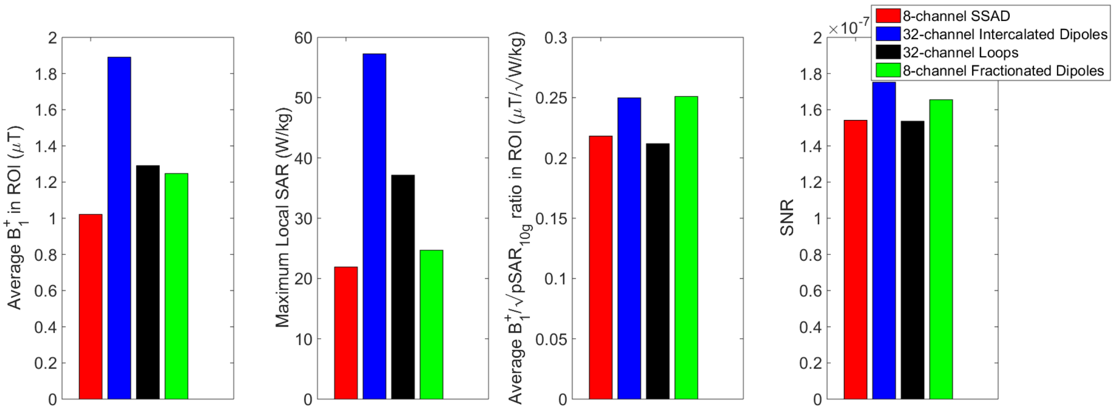

Figure 34: Comparison between the average values of B$_1^+$, peak 10g Averaged SAR, B$_!^+$ over $\sqrt{pSAR10g}$ ratio and SNR on the shimmed 3cm radius sphere at the center of the phantom directly beneath the array (same ROI as in Figure 22) for each of the array designs studied in Step A.

In Figure 34 we can have an overview of the results of Step A. Regarding the transmit performance of the simulated arrays, it is noticeable that when going from and 8-channel SSAD array to a 32-channel miniaturized version, although a great increase in Maximum Local SAR is identifiable, the parallel increase in B$_1^+$ leads to an increased B$_1^+$ over $\sqrt{pSAR10g}$ ratio inside the shimmed ROI. It is important to keep in mind that this increase is also accompanied by an increase in receive performance directly related to the SNR value increase. As for the loop antennas, the small 32-channel version performs worse than the dipole setups in every transmit aspect, and it does not show any increase in its receive capabilities as seen by the SNR values when compared to those of the other arrays.

Apart from the 32-channel intercalated miniaturized dipoles, the 8-channel fractionated setup greatly outperforms all other setups. Although a better transmit and receive performance was obtained with the increased number of channels and size reduction of the dipoles in comparison to the standard 8-channel dipole setup, it still performs almost at the same level as the fractionated dipole antenna 8-channel array both receive and transmit wise.

4.2 Step B: Finding the best morphology

With the conclusions drawn from the first step of the investigation, while still keeping in mind the problems presented in section 2 regarding the fractionated dipole antennas, the next logical step was to try and test this antenna shape as an element for our final goal. This lead to the creation of a higher-density normal-sized fractionated dipole antenna array (with 16 channels), a 32-channel fractionated monopole array and a half-sized fractionated dipole antenna array. All these idealized arrays can be seen in Figure 35 and the corresponding results of the simulations are efficiently summed up in Figure 40. Aditionally, in Figures 36 through 40 we have a visual interpretation of the B_1^+, $\mathrm{B}_1^+/\sqrt{pSAR10g}$, Averaged 10g SAR and SNR data gathered in Figure 40.

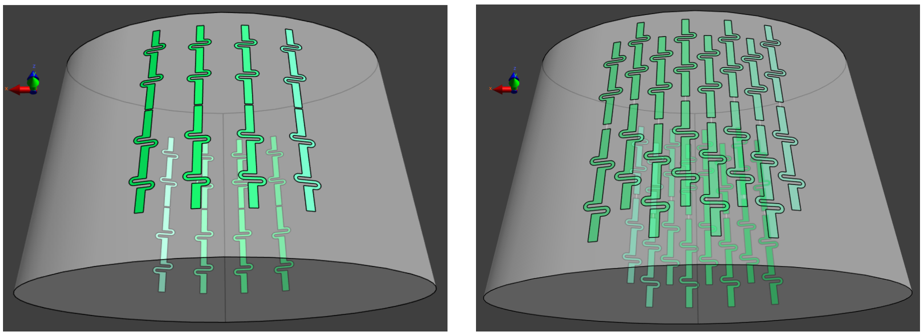

(a) 8-channel fractionated dipole antenna array

(b) 16-channel fractionated dipole antenna array

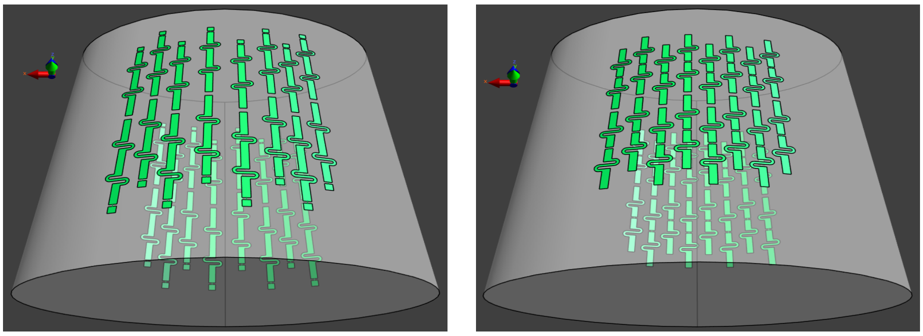

(c) 32-channel fractionated monopole antenna array

(d) 32-channel half-size fractionated dipole antenna array

Figure 35: Sim4Life's python scripting generated geometries of the array designs studied in Step B.

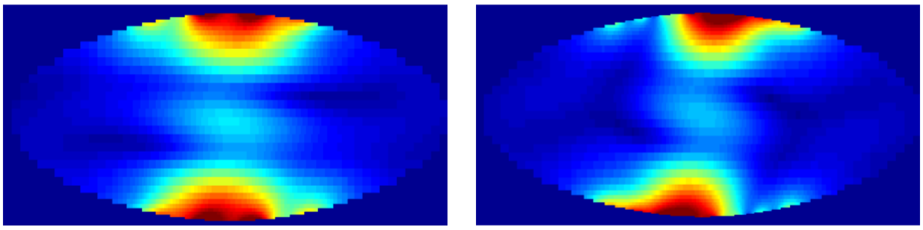

(a) 8-channel fractionated dipole antenna array

(b) 16-channel fractionated dipole antenna array

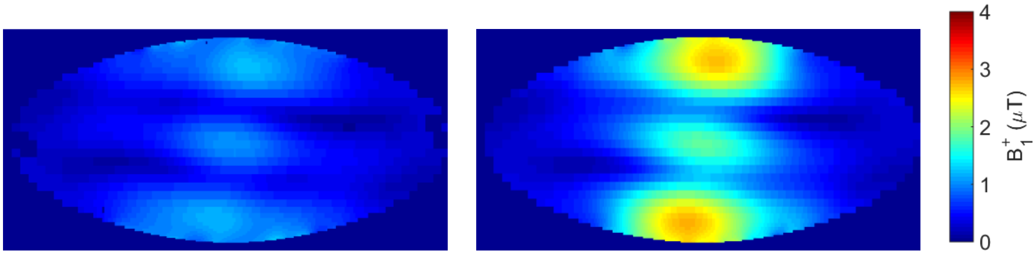

(c) 32-channel fractionated monopole antenna array

(d) 32-channel half-size fractionated dipole antenna array

Figure 36: B_1^+ distributions optimally shimmed through a 3cm radius sphere at the center of the phantom directly beneath the array (same ROI as in Figure 22) for the array designs studied in Step B. All distributions have been normalized to 32W accepted power per array.

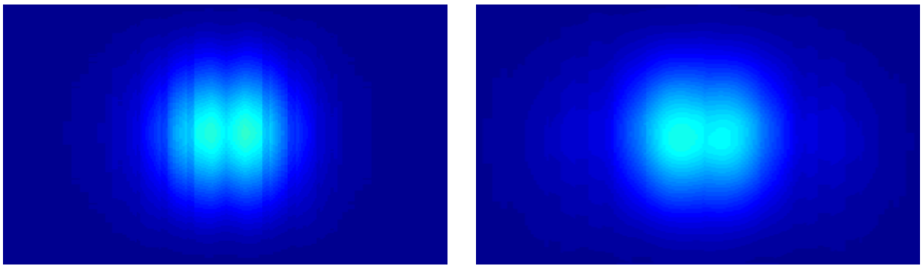

(a) 8-channel fractionated dipole antenna array

(b) 16-channel fractionated dipole antenna array

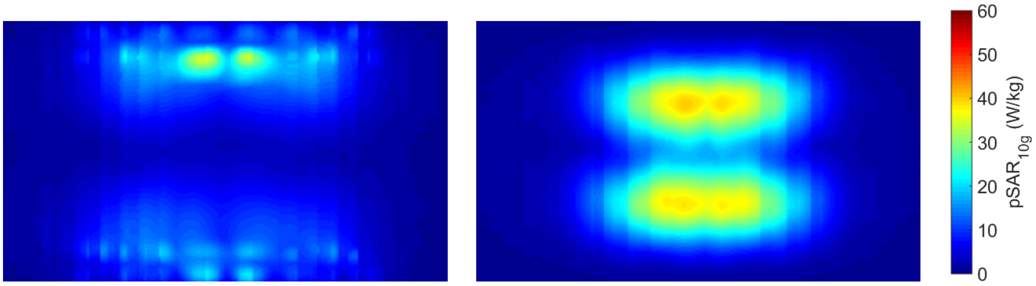

(c) 32-channel fractionated monopole antenna array

(d) 32-channel half-size fractionated dipole antenna array

Figure 37: Coronal maximum intensity projection of the Peak 10g Averaged SAR (pSAR10g) resultant from optimally shimming through a 3cm radius sphere at the center of the phantom directly beneath the array (same ROI as in Figure 22) for each of the array designs studied in Step B.

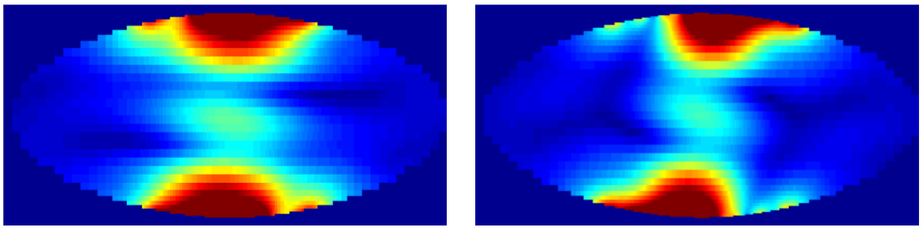

(a) 8-channel fractionated dipole antenna array

(b) 16-channel fractionated dipole antenna array

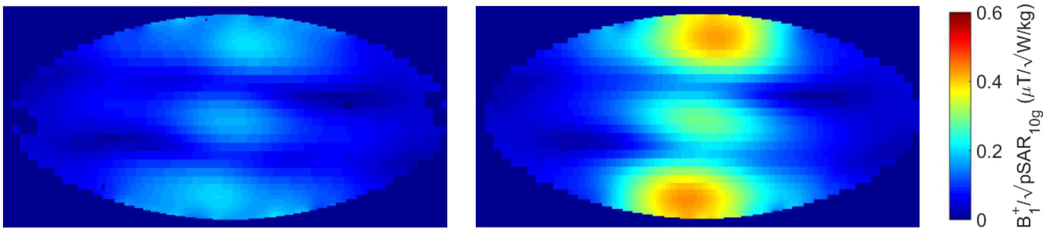

(c) 32-channel fractionated monopole antenna array

(d) 32-channel half-size fractionated dipole antenna array

Figure 38: B_1^+ over $\sqrt{pSAR10g}$ ratio distributions optimally shimmed through a 3cm radius sphere at the center of the phantom directly beneath the array (same ROI as in Figure 22) for each of the array designs studied in Step B.

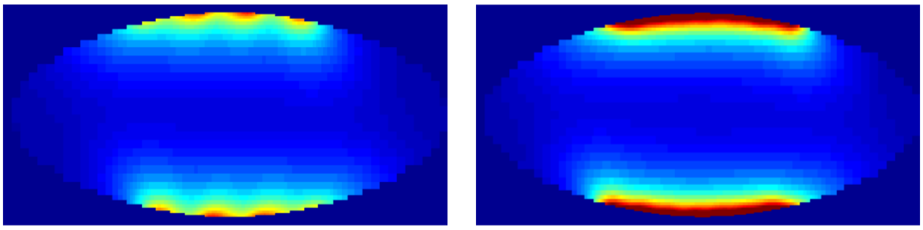

(a) 8-channel fractionated dipole antenna array

(b) 16-channel fractionated dipole antenna array

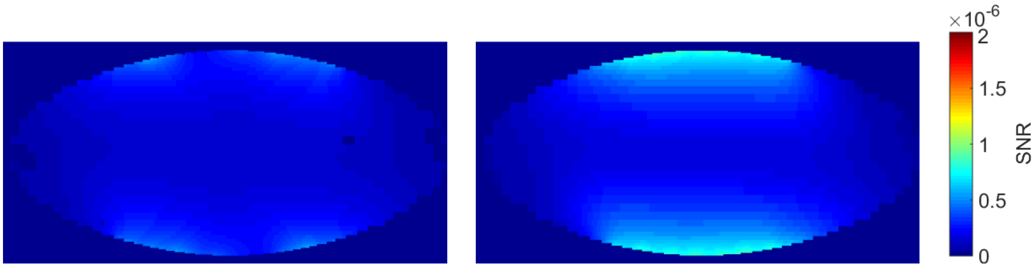

(c) 32-channel fractionated monopole antenna array

(d) 32-channel half-size fractionated dipole antenna array

Figure 39: SNR values for each voxel for each of the array designs studied in Step B.

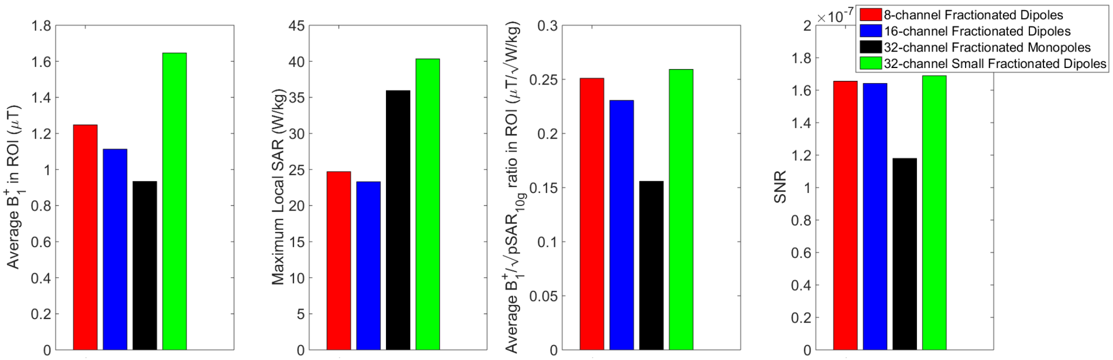

Figure 40: Comparison between the average values of B$_1^+$, peak 10g Averaged SAR, B$_!^+$ over $\sqrt{pSAR10g}$ ratio and SNR on the shimmed 3cm radius sphere at the center of the phantom directly beneath the array (same ROI as in Figure 22) for each of the array designs studied in Step B.

The first two attempts (Figure 35 b) and c)) were not successful, either transmit or receive-wise, when compared to the original 8-channel setup since a clear drop in performance can be seen for every relevant quantity in Figure 40. As for the last test, the 32-channel half-size design (Figure 35 d)), although an increase in the Maximum Local SAR is evident, the increase in B$_1^+$ leads to a slight improvement in the B$_1^+$ over $\sqrt{pSAR10g}$ ratio and consequently of the transmit performance. This slight improvement associated with a noticeable increase in receive efficiency (higher level of SNR) indicates that this geometry might be a good candidate to take through the next step of the investigation.

4.3 Step C: Finding the best placement

With the results of Step B in mind, a final step was taken to fully extend the study to an acceptable broadness. With the 32-channel half-size fractionated dipole antenna displaying promising results and by closely looking at Figure 37d) where the local SAR hotspots are clearly located underneath the central elements of the array, a non-linearly spaced version of the half-size fractionated dipole array was created by spreading the central elements where the local SAR hotspots were identifiable. In theory, this workaround would lower the peak 10g Averaged SAR without drastically affecting the B$_1^+$ and consequentially increase the B$_1^+$ over $\sqrt{pSAR10g}$ ratio performance. In this new version of the half-sized fractionated dipole array, the distance between the outer elements was kept the same while the central ones were placed further away from each other.

In this final step, aiming for the goal of physically building the best performing, simulation-wise, array also two variations (one linearly spaced and one non-linearly spaced), of a 24-channel half-size fractionated dipole antenna array were investigated due to the hardware restraints in scaling up the system to 32-channel stated in section 3, being 24 channels the maximum obtainable channel count for the time window available.

All these last tested geometries can be seen in Figure 41 and the corresponding simulation results are summarized in Figure 46. Additionally, in Figures 42 through 46 we can, once again, have a visual interpretation of the B$_1^+$, B$_1^+/\sqrt{pSAR10g}$, 10g Averaged SAR and SNR distributions.

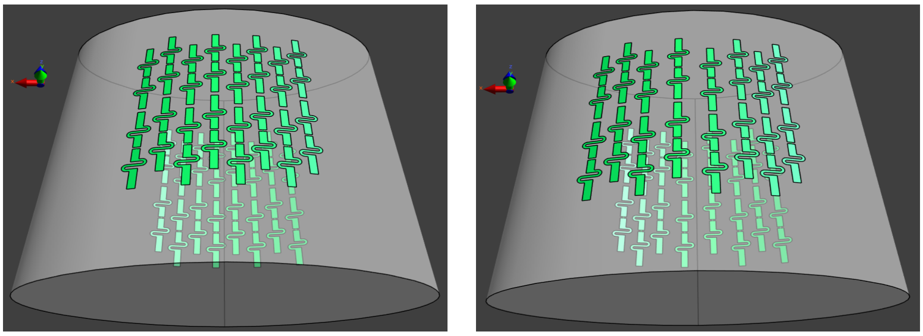

(a) 32-channel half-size fractionated dipole antenna array

(b) 32-channel half-size fractionated dipole antenna array (non-linear spacing)

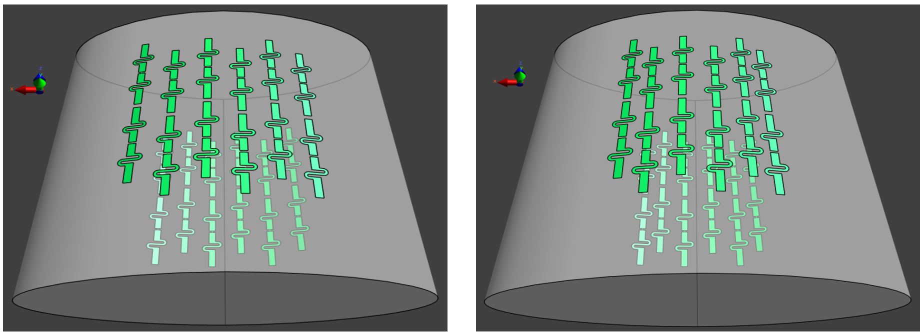

(c) 24-channel half-size fractionated dipole antenna array

(d) 24-channel half-size fractionated dipole antenna array (non-linear spacing)

Figure 41: Sim4Life's python scripting generated geometries of the array designs studied in Step C.

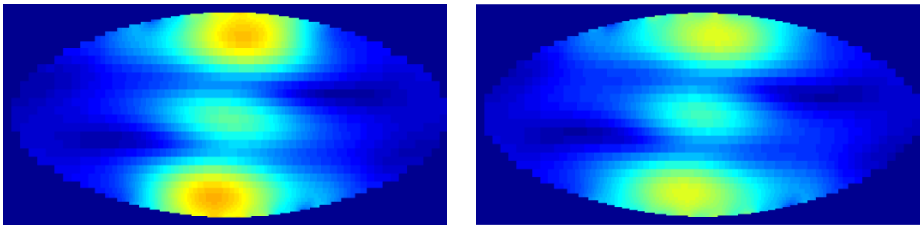

(a) 32-channel half-size fractionated dipole antenna array

(b) 32-channel half-size fractionated dipole antenna array (non-linear spacing)

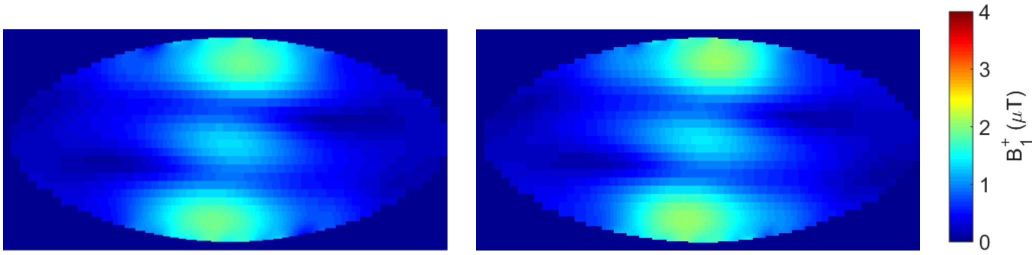

(c) 24-channel half-size fractionated dipole antenna array

(d) 24-channel half-size fractionated dipole antenna array (non-linear spacing)

Figure 42: B_1^+ distributions optimally shimmed through a 3cm radius sphere at the center of the phantom directly beneath the array (same ROI as in Figure 22) for the array designs studied in Step C. All distributions have been normalized to 32W accepted power per array.

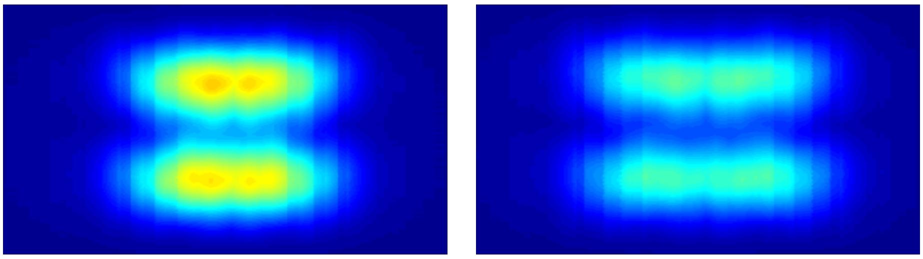

(a) 32-channel half-size fractionated dipole antenna array

(b) 32-channel half-size fractionated dipole antenna array (non-linear spacing)

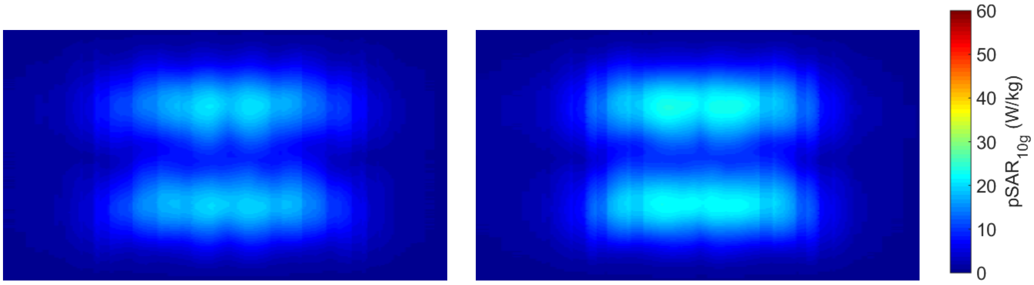

(c) 24-channel half-size fractionated dipole antenna array

(d) 24-channel half-size fractionated dipole antenna array (non-linear spacing)

Figure 43: Coronal maximum intensity projection of the Peak 10g Averaged SAR (pSAR10g) resultant from optimally shimming through a 3cm radius sphere at the center of the phantom directly beneath the array (same ROI as in Figure 22) for each of the array designs studied in Step C.

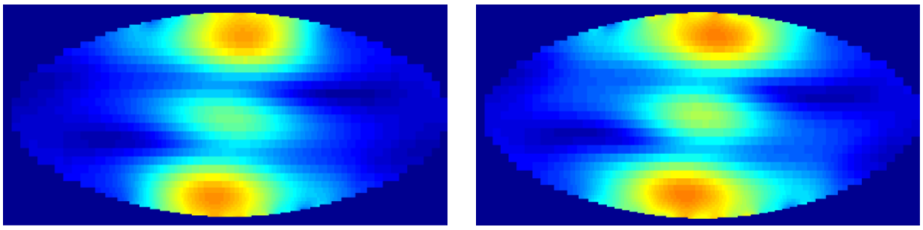

(a) 32-channel half-size fractionated dipole antenna array

(b) 32-channel half-size fractionated dipole antenna array (non-linear spacing)

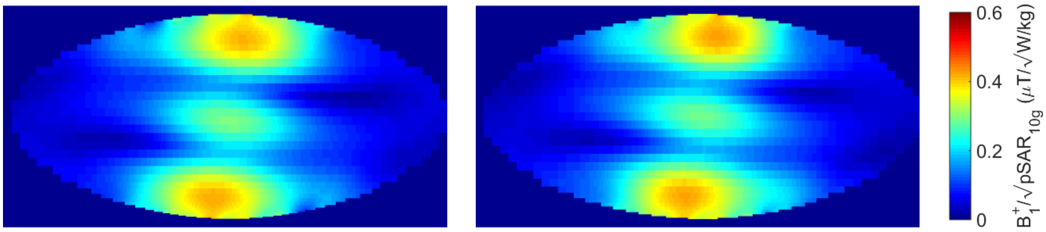

(c) 24-channel half-size fractionated dipole antenna array

(d) 24-channel half-size fractionated dipole antenna array (non-linear spacing)

Figure 44: B_1^+ over $\sqrt{pSAR10g}$ ratio distributions optimally shimmed through a 3cm radius sphere at the center of the phantom directly beneath the array (same ROI as in Figure 22) for each of the array designs studied in Step C.

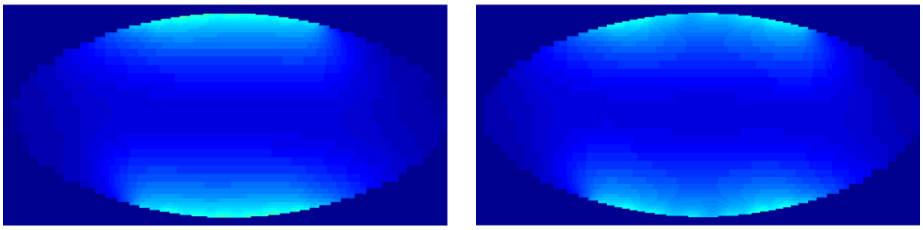

(a) 32-channel half-size fractionated dipole antenna array

(b) 32-channel half-size fractionated dipole antenna array (non-linear spacing)

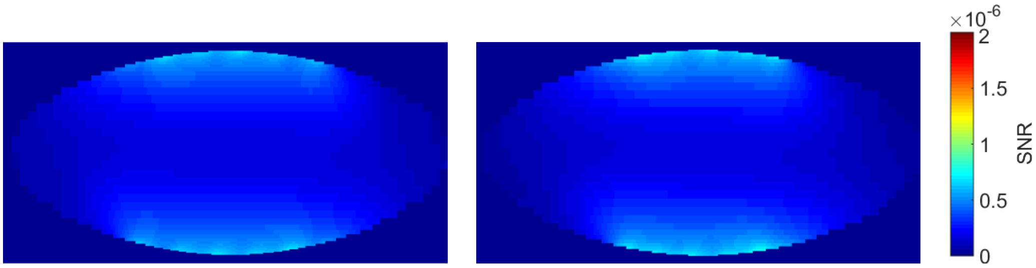

(c) 24-channel half-size fractionated dipole antenna array

(d) 24-channel half-size fractionated dipole antenna array (non-linear spacing)

Figure 45: SNR values for each voxel for each of the array designs studied in Step C.

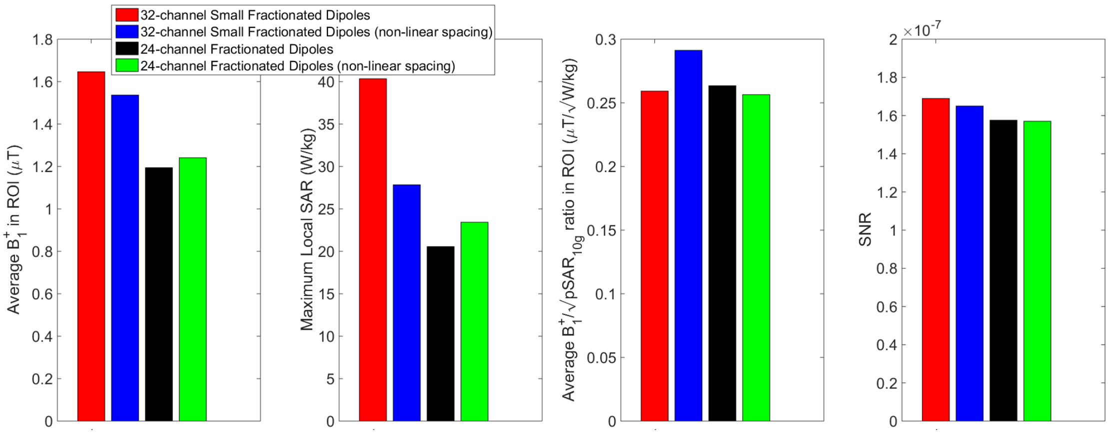

Figure 46: Comparison between the average values of B_1^+, peak 10g Averaged SAR, $\mathrm{B}_!^+$ over $\sqrt{pSAR10g}$ ratio and SNR on the shimmed 3cm radius sphere at the center of the phantom directly beneath the array (same ROI as in Figure 22) for each of the array designs studied in Step C.

Now we can, once more, compare the meaningful variables for the simulated geometries in Step C. It is confirmed that altering the spatial distribution of the 32-channel setup chosen from Step B, although reducing B_1^+ along side the Maximum Local SAR, leads to an improved B_1^+ over $\sqrt{pSAR10g}$ ratio and transmit performance nonetheless, while maintaining practically the same SNR value. As for the the 24-channel setups, in this particular case, the performance, as expected, was lower than the 32-channel setup in all aspects.

Although the SAR hotspot pattern was not identifiable in the 24-channel setup as it was in the 32-channel for the sake of workflow the non-linear spacing was also applied to the 24-channel configuration and yielded worse results than the linearly spaced one, leading to the conclusion that this geometrical rearrangement is only viable for cases where the SAR hotspots are clearly identifiable in the SAR maximum intensity projections.

4.4 The best performing array

To finalize the analysis of the simulations performed on phantoms it is reasonable to compare the starting point of the fractionated dipole antennas (the 8-channel setup) with the best performing array (the 32-channel half-size setup with non-linear spacing). All the previously compared parameters were observed with the addition of the pSAR10g over B_1^+ ratio that reminds us that a 10% increase in the B_1^+ over pSAR10g ratio corresponds to a 20% decrease in pSAR10g.

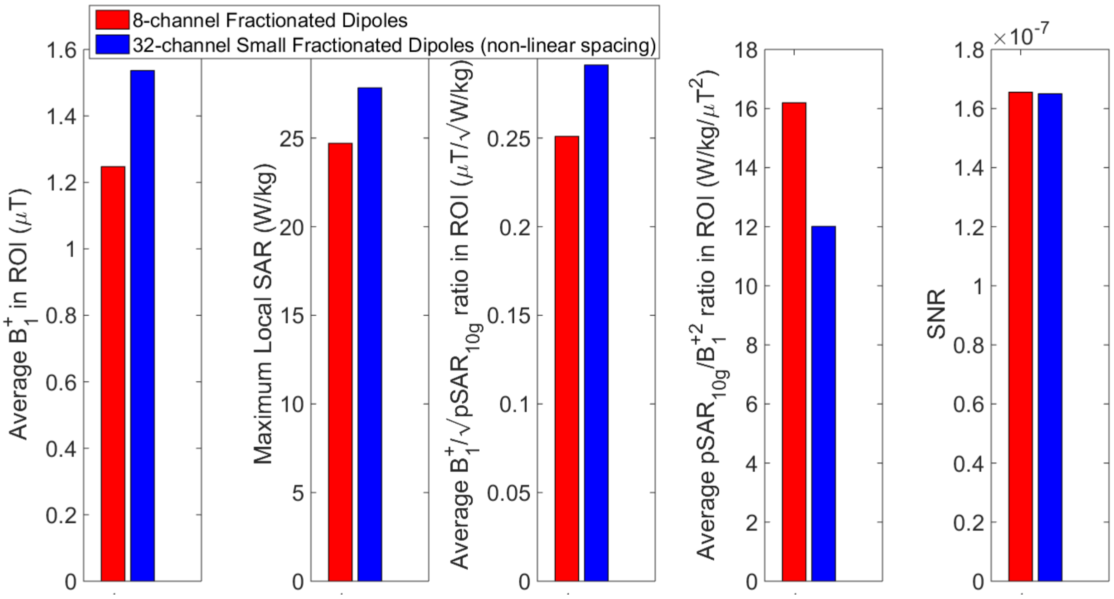

Figure 47: Comparison between the average values of B$_1^+$, peak 10g Averaged SAR, B$_!^+$ over $\sqrt{pSAR10g}$ ratio, pSAR10g over B$_!^+$2 ratio and SNR on the shimmed 3cm radius sphere at the center of the phantom directly beneath the array (same ROI as in Figure 22) for the 8-channel fractionated dipole antenna array and the 32-channel half-size fractionated dipole antenna array with non-linear spacing.

In figure 47 we can summarize all improvements obtained by going from the traditional 8-channel setup to the 32-channel half-sized fractionated dipole. An approximate increase of 23% in B$_1^+$ although accompanied by an increase of approximately 12% in peak 10g Averaged SAR, leads to an overall increase of the transmit performance ratio of about 16% while maintaining the same SNR and consequentially the same receive performance.

Another factor to corroborate the implementation of the idealized optimal array, although beyond the scope of this project, is the increased acceleration performance associated with the parallel imaging capabilities unlocked by a higher number of channels available. Parallel imaging is a complex but well-established technique. In general, it performs better with more elements but the acceleration that can be achieved depends also on the individual fields. Its performance is usually represented by spatial distributions of the so-called geometry-factor that indicates at each point how much extra noise penalty the acceleration will provide. However, this is beyond the scope of this project and although the general trend is the increase of acceleration performance with a higher number of channels, in any future work, a thorough inspection of the individual fields must be performed before drawing any definite conclusions.

With all the mentioned factors combined and, keeping in mind the hardware restrictions that forces the array to be set to 24-channels, a 24-channel half-size and linearly spaced fractionated dipole antenna array has been elected as the array to be built and tested.

4.5 Verification on a human model

As a final step, the array that was chosen to be built for scanner testing was once again simulated using SIM4LIFE (Zurich MedTech, Zurich, Switzerland) on a human model, named Duke, in order to have some notions of the behaviour of the array when applied to a non-homogeneous density/conductivity system.

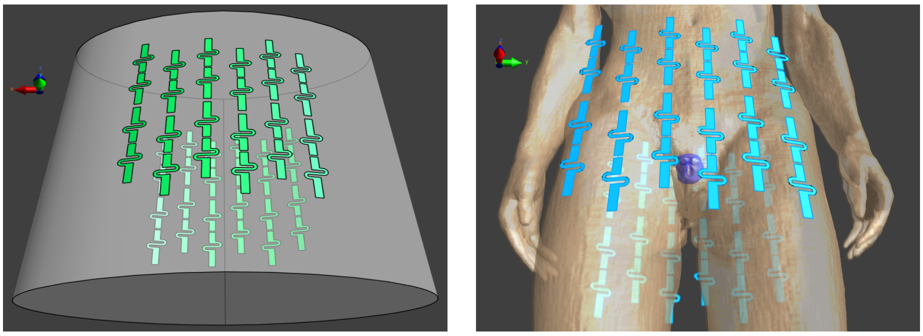

(a) 24-channel half-size fractionated dipole antenna array

(b) 24-channel half-size fractionated dipole antenna array

Figure 48: Sim4Life's python scripting generated geometries of the 24-channel half-size linearly spaced fractionated dipole antenna array when placed on a homogeneous phantom and on the human model Duke.

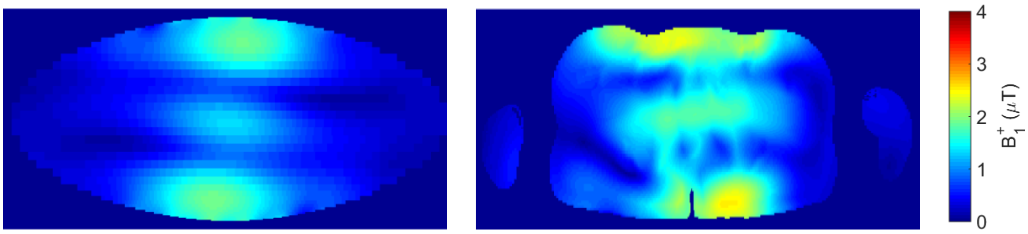

(a) 24-channel half-size fractionated dipole antenna array

(b) 24-channel half-size fractionated dipole antenna array

Figure 49: B_1^+ distributions optimally shimmed through a 3cm radius sphere at the center of the phantom directly beneath the array (same ROI as in Figure 22 on Phantom) and a 3cm radius sphere with centre coincident with the prostate's centre (on Duke) for the 24-channel half-size linearly spaced fractionated dipole antenna array when placed on a homogeneous phantom and on the human model Duke. All distributions have been normalized to 32W accepted power per array.

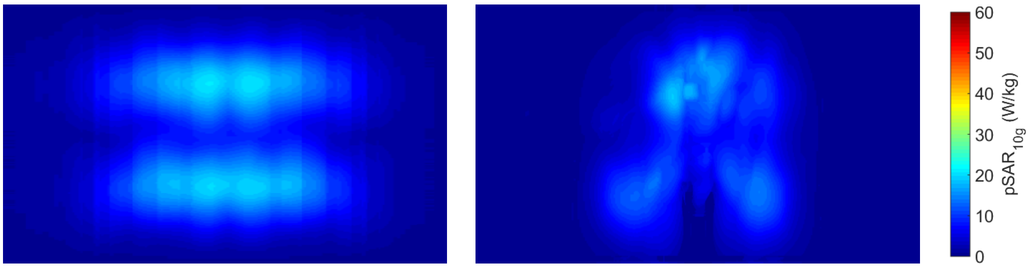

(a) 24-channel half-size fractionated dipole antenna array

(b) 24-channel half-size fractionated dipole antenna array

Figure 50: Coronal maximum intensity projection of the Peak 10g Averaged SAR (pSAR10g) resultant from optimally shimming through a 3cm radius sphere at the center of the phantom directly beneath the array (same ROI as in Figure 22 on Phantom) and a 3cm radius sphere with centre coincident with the prostate's centre (on Duke) for the 24-channel half-size linearly spaced fractionated dipole antenna array when placed on a homogeneous phantom and on the human model Duke.

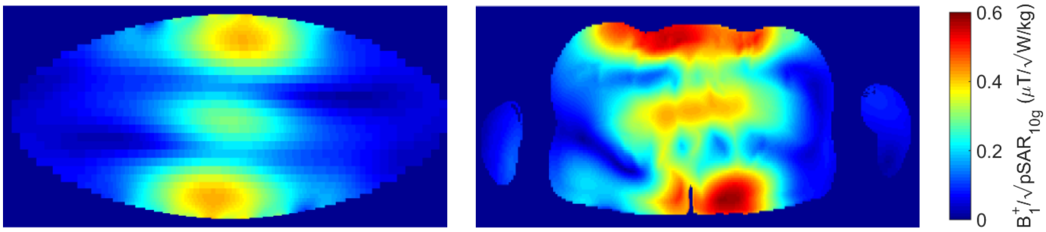

(a) 24-channel half-size fractionated dipole antenna array

(b) 24-channel half-size fractionated dipole antenna array

Figure 51: B_1^+ over $\sqrt{pSAR10g}$ ratio distributions optimally shimmed through a 3cm radius sphere at the center of the phantom directly beneath the array (same ROI as in Figure 22 on Phantom) and a 3cm radius sphere with centre coincident with the prostate's centre (on Duke) for the 24-channel half-size linearly spaced fractionated dipole antenna array when placed on a homogeneous phantom and on the human model Duke.

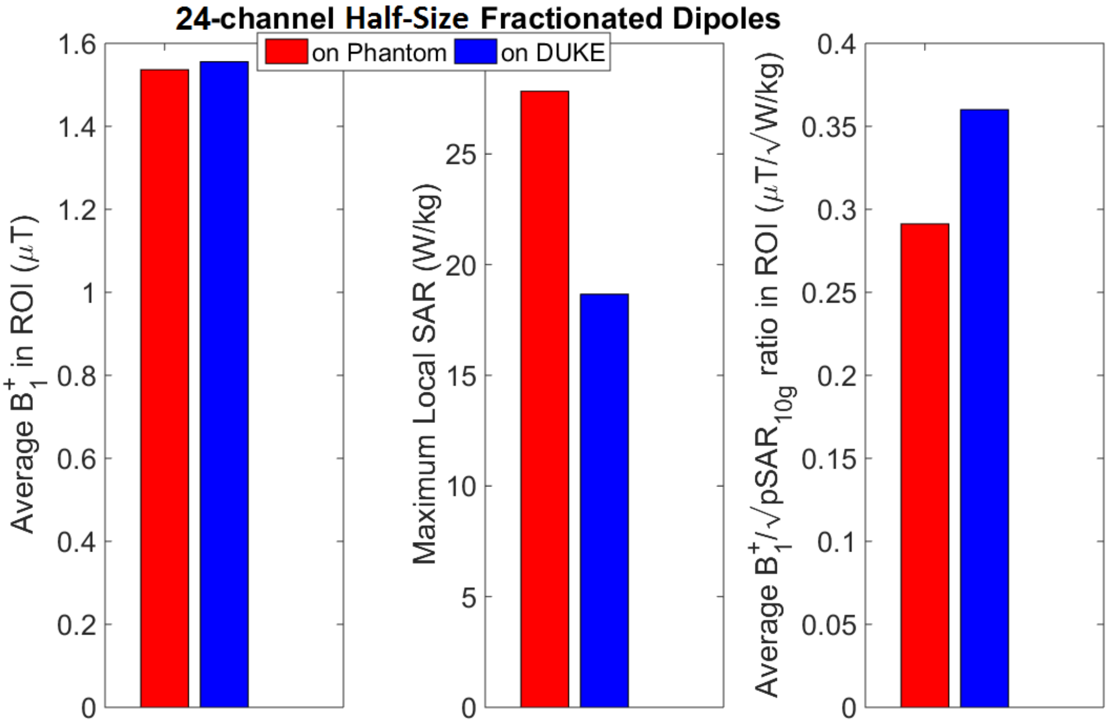

Figure 52: Comparison between the average values of B_1^+, peak 10g Averaged SAR and B_1^+ over $\sqrt{pSAR10g}$ ratio on the shimmed 3cm radius sphere at the center of the phantom directly beneath the array (same ROI as in Figure 22 on Phantom) and a 3cm radius sphere with centre coincident with the prostate's centre (on Duke) for the 24-channel half-size linearly spaced fractionated dipole antenna array when placed on a homogeneous phantom and on the human model Duke.

In figure 52 a comparison between the studied parameters was made between the 24-channel half-size fractionated dipole antenna array setup on the phantom used throughout the entire study and on Duke, the realistic model of a male human body. The B_1^+ values are kept at the same level but the peak 10g Averaged SAR decreases by approximately 30% leading to a logical increase in the B_1^+ over peak SAR ratio. It is important to refer to the absence of SNR analysis in this case due to computational issues arisen from the more than tenfold increase in voxelized cells when switching from the ellipsoid phantom to the human model, Duke. The machine available for SNR calculations did not have the requirements to withstand the increase in computational load.

Although in this particular case the results strongly indicate the performance on a human body is higher than when tested on a phantom, it is necessary to always confirm this pattern when testing a new array in order to have a realistic overview of its performance on a human body.

4.6 7T scanner tests

Having built and matched the 24-channel half-size fractionated dipole antenna array, it was possible to test it inside the 7 Tesla scanner available in the UMCU according to the setup described in section 3 and depicted in Figure 28.

Scanning efficiently and analysing the performance of the array was not the aim of these tests. They were solely performed as a feasibility study and a proof-of-principle in order to assess if the array was operational for transmit-receive environments and viable for further perfection and development.

With this in mind, several simple scans were performed on the 23-channel set up, one less than simulated due to the phantom limitations described in section 3.

In Figure 53 it is possible to see in a) signal being received by the array and in b) the transmit field of the array. It is also important to state that due to the imperfections inherent to the 16-channel transmit-receive switch box used in the scans, power was not evenly distributed throughout the 23 channels having eight channels being driven at 1000W, eight more at 1400W, four at 700W, one at 350W, one at 250W and one at 160W.

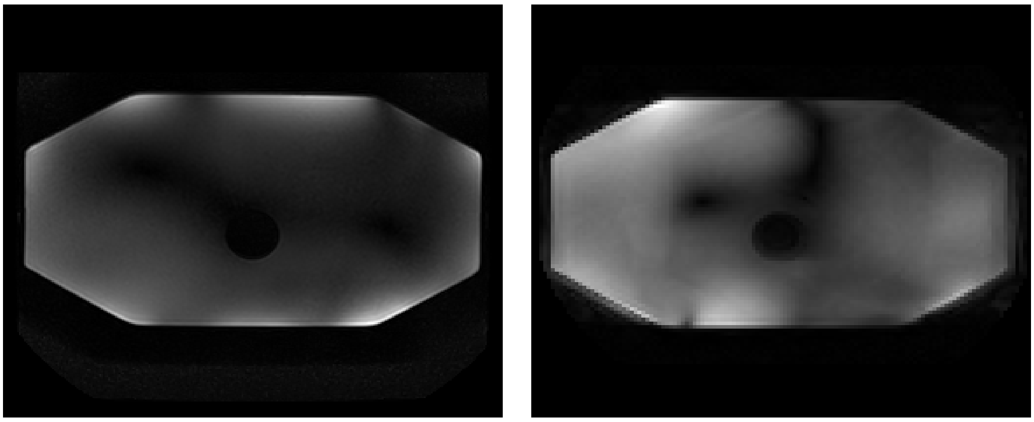

(a) Receive performance (b) Transmit performance

Figure 53: Performance of the scanner tested array on an octagonal shaped ethylene glycol phantom with an empty tube in the central portion. a) survey scan; b) DREAM B1 map.

5 Conclusion

The aim of this project was born from the evidence that all SAR hotspots in multi-channel arrays are mainly located underneath each element. This lead to the speculation that by spreading the input power of the array over a greater number of smaller elements would lead to a increase in transmit performance without losing receive capabilities.

From early in the project it could easily be seen that this hypothesis was not universally applicable and that the behaviour of the different arrays would vary depending on the shape and spatial distribution of the several elements. Nonetheless, improvement of performance by using a greater number of smaller elements was still believed to be achievable.

With this in mind, a rigorous simulation protocol was set as standard for all future simulations and was applied to several different element shapes and array spatial arrangements, during the search for a good massively parallel transmit array. This simulation protocol was initially applied to a plethora of dipole antenna array designs, which were further ahead discarded as a solution to our problem. As a second step, after implementing a loop decoupling step to the simulation protocol, an optimized loop array was tested and rendered unfit for a massively parallel transmit array. Finally, the original protocol was applied to several variations of fractionated dipole antenna arrays.

These final tests, with the fractionated dipole antennas, led to the conclusion that a 32-channel half-size fractionated dipole antenna array was the candidate that better achieved what was idealized as a good performance for a massively parallel transmit array. It achieved a higher value for the B_1^+ over $\sqrt{pSAR_{10g}}$ ratio, which translates into a higher transmit performance without losing receive capabilities.

These results show that a massively parallel transmit array approach, although still in an early stage of research, is a good path to follow in order to further develop surface arrays for MR imaging at high fields.

Results that fully justify the extensive investment that a transition to massively parallel transmit arrays would require have not been achieved during this study but the results obtained surely give a green light to start a more extended line of research regarding this topic. In order to prove that the development of massively parallel transmit arrays is beneficial, any future work regarding this topic must encompass three key points. First, although in this study a 20% reduction in SAR was achieved, the influence on array performance of the geometry and positioning of the arrays in a simulation based environment can still be further investigated, preferably on human models. Second, it should focus on performing more rigorous scanning tests following what is commonly seen in transceive array testing in the MR community, namely more elaborate B_1 maps and receive performance checks, and attempt in-vivo imaging. The last key point requires an investigation on the impact of massively parallel imaging arrays on imaging acceleration.

If the focus of future research is set on these three points and all of them yield positive results, the concept of a massively parallel transmit array can be implemented as a go-to solution for high field MR imaging.

A All Dipole tests

Before the intercalated dipole array was identified as the best candidate to represent the regular dipole in a massively parallel transmit array, a plethora of other scenarios were considered. The comparison between all the simulated scenarios can be seen in Figure 54 in a simplistic manner, only looking at the B_1^+ over $\sqrt{pSAR_{10g}}$ ratio.

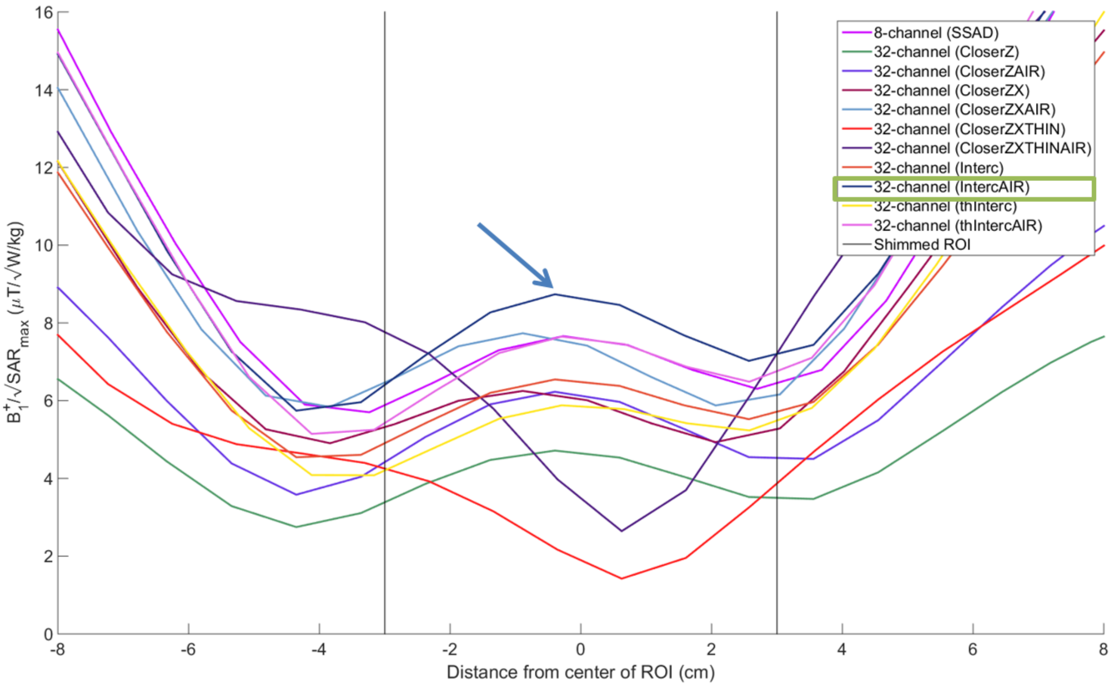

Figure 54: B_1^+ over $\sqrt{pSAR_{10g}}$ ratio of all testes dipole array variations on a line along the y-axis passing through the center of the phantom.

In this picture we can clearly identify that the IntercAIR simulation (Intercalated Dipole on air, with no substrate) was the best performing array with regular dipoles and thus the geometry used for reference in section 4.

B Code

B.1 Extracting B1 Fields - Sim4Life

```python
import s4l_v1 as s4l
from scipy.io import savemat
import s4l_v1.simulation.emfdtd as fdtd
import numpy
import sys, os
from pylab import *

sims = s4l.simulation.GetSimulations()

ii = 0
sim = sims[ii]
results = sim.Results
nports = 24 #Select amount of ports you want to extract
for jj in range(0,nports):

        result = results(jj)

        #Extract field sensor
        overall_field_sensor = result['SensBox']
        input_power_sensor = result['Input Power']

        #Extract power for current port
        Psensor = input_power_sensor['EM Input Power(f)']
        Psensor.Update()
        P = Psensor.Data.GetComponent(0)

        B1 = overall_field_sensor['B1(x,y,z,f0)'] # Extract B1 Field
        B1data = B1.Data # Contains grid and field (and other stuff)
        B1grid = B1data.Grid # Select grid data
        xaxis = B1grid.XAxis
        yaxis = B1grid.YAxis
        zaxis = B1grid.ZAxis
        B1.Update()

        #Normalize B1 to 32W total array power
        B1field_unshaped = B1data.Field(0) # Select B1 field from all data
        B1field_normalized = (B1field_unshaped/sqrt(P))*sqrt(4/3)#*2#*sqrt(2)

        #Exporting path
        path = r'D:\\Data\\DUKE - 4th Part\\
```

```
        B1_24xSmallFracD_onDUKE\\'
        mdict = {'Snapshot0':B1field_normalized, 'Axis0':xaxis, 'Axis1':yaxis, 'Axis2':zaxis}
        ext = '.mat'
        savemat(path+sim.Name+str(jj+1)+ext,mdict)
```

B.2 B_1^+ Shimming - MATLAB

```
function [B1_shimmed_sum,x1,B1_minus_sum] = ampShim(nports,xmid,ymid,zmid)
    %GET RAW TRANSMIT FIELDS (B1)
    data = getAllDistributionsFromFile;

    %CREATE MASK AND INITIAL CONDITIONS FOR THE OPTIMIZATION PROBLEM
    [tDmask, X0, Nreps] = prepareRFamps(data,xmid, ymid, zmid);

    %SOLVE THE OPTIMIZATION PROBLEM
    x1 = optimizeRFamps(data.B1.B1plus, tDmask,0,'Max',X0,Nreps);

    %SHIM THE RAW TRANSMIT FIELDS WITH THE OBTAINED VALUES
    for ii = 1:nports
        B1_shimmed(:,:,:,ii) = data.B1.B1plus(:,:,:,ii)*x1(ii);
        B1_minus(:,:,:,ii) = data.B1.B1minus(:,:,:,ii)*x1(ii);
    end

    %SUM OVER NUMBER OF SIMULATED CHANNELS
    B1_shimmed_sum = sum(B1_shimmed,4);
    B1_minus_sum = sum(B1_minus,4);

    %DISPLAY THE SHIMMED B1+ DISTRIBUTION
    B1_slice = squeeze(abs(B1_shimmed_sum(:,ymid,:)));
    visualizeDistr2(B1_slice,data.B1.axes.x, data.B1.axes.z)

    max(max(B1_slice))
    figure; visualizeDistr2(abs(B1_shimmed_sum(:,:,zmid)),data.B1.axes.x, data.B1.axes.y)
end
```

B.3 10g Averaged SAR Calculation - Sim4Life

```
import s4l_v1 as s4l
import scipy.io
import numpy
import scipy.linalg
from numpy import linalg as LA
import numpy.matlib

```

```
#Averaging over 10g cubes
def Average(W,cube,E):
        xl = cube.Lower[0]
        xu = cube.Upper[0]
        yl = cube.Lower[1]
        yu = cube.Upper[1]
        zl = cube.Lower[2]
        zu = cube.Upper[2]
        return sum(sum(sum(W*E[zl:zu+1,yl:yu+1,xl:xu+1],0),0),0)/cube.Volume

#Gets the weights of each 10g cube per voxel index
def getWeights(cube):
        W = zeros((3,2))
        LL=grid.GetPoint(grid.GetCellPoints(grid.ComputeCellIndex(cube.Lower[0],cube.Lower[1],cube.Lower[2]))[0])
        LU=grid.GetPoint(grid.GetCellPoints(grid.ComputeCellIndex(cube.Lower[0],cube.Lower[1],cube.Lower[2]))[7])
        for ii in range(3):
                W[ii,0] = (LU-cube.Point0)[ii]/(LU-LL)[ii]
        UL=grid.GetPoint(grid.GetCellPoints(grid.ComputeCellIndex(cube.Upper[0],cube.Upper[1],cube.Upper[2]))[0])
        UU=grid.GetPoint(grid.GetCellPoints(grid.ComputeCellIndex(cube.Upper[0],cube.Upper[1],cube.Upper[2]))[7])
        for ii in range(3):
                W[ii,1] = (cube.Point1-UL)[ii]/(UU-UL)[ii]

        xw =[W[0,0]]+list(numpy.ones(cube.Upper[0]-cube.Lower[0]-1))+[W[0,1]]
        yw =[W[1,0]]+list(numpy.ones(cube.Upper[1]-cube.Lower[1]-1))+[W[1,1]]
        zw =[W[2,0]]+list(numpy.ones(cube.Upper[2]-cube.Lower[2]-1))+[W[2,1]]
        W = numpy.meshgrid(zw,yw,xw,indexing='ij')
        W = W[0]*W[1]*W[2]
        W3 = zeros(list(W.shape))
        W3[:,:,:] = W
        return W3

#Input shim values from MATLAB
shim = [1.0000 + 0.0000j,
        0.8048 + 0.5935j,
        0.4500 + 0.8930j,
        -0.1348 + 0.9909j,
```

```
        0.9919 - 0.1268j,
        -0.5803 - 0.8144j,
        -0.8405 - 0.5418j,
        -0.6985 - 0.7156j,
        -0.9843 - 0.1765j,
        -0.8069 - 0.5907j,
        -0.4647 - 0.8855j,
        0.1611 - 0.9869j,
        -0.9971 + 0.0756j,
        0.6950 + 0.7190j,
        0.9219 + 0.3875j,
        0.7204 + 0.6935j,
        0.9989 - 0.0478j,
        0.8932 + 0.4497j,
        0.5690 + 0.8223j,
        -0.0286 + 0.9996j,
        0.9510 - 0.3091j,
        -0.8169 - 0.5768j,
        -0.9317 - 0.3633j,
        -0.7512 - 0.6600j,
        -0.9997 - 0.0225j,
        -0.8947 - 0.4466j,
        -0.5505 - 0.8348j,
        0.0340 - 0.9994j,
        -0.9630 + 0.2696j,
        0.8890 + 0.4579j,
        0.9550 + 0.2965j,
        0.8187 + 0.5743j]

order = ['P01', 'P02', 'P03', 'P04',
         'P05', 'P06', 'P07', 'P08',
         'P09', 'P10', 'P11', 'P12',
         'P13', 'P14', 'P15', 'P16',
         'P17', 'P18', 'P19', 'P20',
         'P21', 'P22', 'P23', 'P24',
         'P25', 'P26', 'P27', 'P28',
         'P29', 'P30', 'P31', 'P32',]

S = numpy.zeros([32,32],'complex')
a = numpy.zeros(32,'complex')
z = numpy.zeros(32,'complex')
z0 = 50
sim = s4l.simulation.GetSimulations()[1]
print(sim.Name)
multresults = sim.Results()
order2 = multresults.keys()

for ii in range(32):
```

```
    results = multresults.GetSimulation(order2[ii])

    P = numpy.zeros(32,'complex')

    # Get power for current port
    input_power_sensor = results['Input Power']
    Psensor = input_power_sensor['EM Input Power(f)']
    Psensor.Update()
    P[ii] = Psensor.Data.GetComponent(0)

    sensor = results.GetSensor('SensBox')
    fieldclass = sensor.GetData('EM E(x,y,z,f0)')
    Efield = fieldclass.Field(0)
    grid = fieldclass.Grid
    new_shape = (fieldclass.Grid.Dimensions[2]-1, fieldclass.Grid.Dimensions[1]-1, fieldclass.Grid.Dimensions[0]-1)
    if ii == 0:
        Eall = numpy.zeros(list(Efield.shape),'complex')
        Ec = numpy.zeros(list(Efield.shape)+[32],'complex')
        Ecs = numpy.zeros(list(Efield.shape)+[32],'complex')
        sar = sensor.GetData('SAR(x,y,z,f0)')
        ld = sensor.GetData('El. Loss Density(x,y,z,f0)')
        rho = ld.Field(0)/sar.Field(0)
        rho = [rho[x] if numpy.isnan(rho[x]) == False else 0 for x in range(size(rho))]
        rho = numpy.asarray(rho)
        Ex = Efield[:,0]
        Ey = Efield[:,1]
        Ez = Efield[:,2]
        Eabs = (numpy.abs(numpy.sqrt(Ex*Ex.conj()+Ey*Ey.conj()+Ez*Ez.conj()))).flatten()
        sig = 2*(ld.Field(0)).flatten()/(numpy.power(Eabs,2))
        mask = [1 if x>0 else 0 for x in sig]
        mask = numpy.asarray(mask)
        x = grid.XAxis
        y = grid.YAxis
        z = grid.ZAxis
        del Eabs
        del ld
        del sar
        volmesh = numpy.meshgrid(numpy.diff(z),numpy.diff(y),numpy.diff(x), indexing='ij')
```

```
                vol = volmesh[0].flatten()*volmesh[1].flatten()*volmesh[2].flatten()
                vol = numpy.asarray(vol)

        #Normalize E-fields to 32W total array accepted power
        Ec[:,:,ii] = Efield/(numpy.sqrt(P[ii]))*zip(mask,mask,mask)
        Ecs[:,:,ii] = Ec[:,:,ii]*shim[ii]

        del Efield
        del fieldclass
        del sensor
        # del i
        # del v
        # del results


Eall[:,:] = Ecs[:,:,0] + Ecs[:,:,1] + Ecs[:,:,2] + Ecs[:,:,3] + Ecs[:,:,4] + Ecs[:,:,5] + Ecs[:,:,6] + Ecs[:,:,7] + Ecs[:,:,8] + Ecs[:,:,9] + Ecs[:,:,10] + Ecs[:,:,11] + Ecs[:,:,12] + Ecs[:,:,13] + Ecs[:,:,14] + Ecs[:,:,15] + Ecs[:,:,16] + Ecs[:,:,17] + Ecs[:,:,18] + Ecs[:,:,19] + Ecs[:,:,20] + Ecs[:,:,21] + Ecs[:,:,22] + Ecs[:,:,23] + Ecs[:,:,24] + Ecs[:,:,25] + Ecs[:,:,26] + Ecs[:,:,27] + Ecs[:,:,28] + Ecs[:,:,29] + Ecs[:,:,30] + Ecs[:,:,31]
del Ecs
del Ec

results = multresults.GetSimulation(multresults.keys()[1])

fieldclass = results.GetSensor('SensBox')

grid = fieldclass.GetData('EM E(x,y,z,f0)').Grid

import EmPostPro
cubes, lossyrho_fd, labels_fd = EmPostPro.ConstMassCubesGenerator.Generate(grid, target_mass_kg=1E-2, enable_uncertainty_region=False)
print(len(cubes))

LUT = numpy.zeros(len(cubes))
for ii in range(len(cubes)):
        LUT[ii] = cubes[ii].ReferenceCellId

#Calculate point SAR
SAR = numpy.zeros((Eall.shape[0]),'complex')
for i in range(Eall.shape[0]):
                if sig[i] != 0.0:
```

```
            e = Eall[i]
            SAR[i] = (sig[i]/(2*rho[i]))*numpy.dot(e.conj().transpose(),e)*vol[i]
            del e

del Eall
del sig
del vol

#Caclulate 10g Averaged SAR
SAR = SAR.reshape(list((grid.ZAxis.size-1,grid.YAxis.size-1,grid.XAxis.size-1)))
SAR10g = numpy.zeros([len(cubes)])
for ii in range(len(cubes)):
    print(ii)
    if (cubes[ii].Lower[2]!=cubes[ii].Upper[2] and cubes[ii].Lower[1]!=cubes[ii].Upper[1] and cubes[ii].Lower[0]!=cubes[ii].Upper[0]):
        SAR10g[ii] = Average(getWeights(cubes[ii]),cubes[ii],SAR)



# path = r'D:\\Data\\Frac - 3rd Part\\SAR_OPTSHIM\\SAR10g_32xIntercDipstest'
path = r'D:\\Data\\Loops - 2nd Part\\SAR_OPTSHIM\\SAR10g_32xLoopsStraighttest'

mdict = {'SAR10g':SAR10g, 'LUT':LUT}
scipy.io.savemat(path,mdict)

del SAR
del SAR10g
```

B.4 Noise Covariance Matrix Calculation - Sim4Life

```
import s4l_v1 as s4l
from scipy.io import savemat
import s4l_v1.simulation.emfdtd as fdtd
import numpy as np
import sys, os
from pylab import *
from scipy import interpolate

sims = list(s4l.document.AllSimulations)

kk = 0
sim = sims[kk]
results = sim.Results()
```

```

nports = 32 #Select amount of ports you want to extract

# Extract initial results to calculate conductivity

result_ini = results.GetSimulation(results.keys()[0])
overall_field_sensor_ini = result_ini['SensBox']
fieldclass_ini = overall_field_sensor_ini.GetData('EM E(x,y,z,f0)')
Efield_ini = fieldclass_ini.Field(0)
ld_ini = overall_field_sensor_ini.GetData('El. Loss Density(x,y,z,f0)')
Ex_ini = Efield_ini[:,0]
Ey_ini = Efield_ini[:,1]
Ez_ini = Efield_ini[:,2]
Eabs_ini = (numpy.abs(numpy.sqrt(Ex_ini*Ex_ini.conj()+Ey_ini*Ey_ini.conj()+Ez_ini*Ez_ini.conj()))).flatten()

term1 = 2*(ld_ini.Field(0)).flatten()
term2 = (numpy.power(Eabs_ini,2))

sig = np.divide(term1,term2)
sig = np.nan_to_num(sig) #Remove potential nans created by dividing by zero

Efield = overall_field_sensor_ini['EM E(x,y,z,f0)']
Edata_ini = Efield.Data
Egrid_ini = Edata_ini.Grid

xaxis = Egrid_ini.XAxis
yaxis = Egrid_ini.YAxis
zaxis = Egrid_ini.ZAxis

dx = np.diff(xaxis)
dy = np.diff(yaxis)
dz = np.diff(zaxis)

DX,DY,DZ = meshgrid(dx,dy,dz)
V_matrix = DX*DY*DZ # Matrix containing volume of every single voxel
V_matrix = np.transpose(V_matrix,(1,0,2)) #Reshape field to match shape E-field

new_shape = (Egrid_ini.Dimensions[0]-1, Egrid_ini.Dimensions[1]-1, Egrid_ini.Dimensions[2]-1)
sig_reshaped = sig.reshape((new_shape[0],new_shape[1],new_shape[2]),order='F')

```

```
R_matrix = np.zeros([nports,nports],dtype='complex') # Noise covariance matrix. Will be filled in for loop.
# P = np.zeros(nports,'complex')
for ii in range(1,nports+1):

    result_ii = results.GetSimulation(results.keys()[ii-1])

    overall_field_sensor_ii = result_ini['SensBox']

    fieldclass_ii = overall_field_sensor_ii.GetData('EM E(x,y,z,f0)')
    Efield_ii = fieldclass_ii.Field(0)

    Ex_ii = Efield_ii[:,0]
    Ey_ii = Efield_ii[:,1]
    Ez_ii = Efield_ii[:,2]

    # Extract current for every port for subsimulation ii
    i_ii = result_ii.GetSensor(result_ii.keys()[ii]).GetData('EM I(f)').GetComponent(0)


    for jj in range(1,nports+1):
        result_jj = results.GetSimulation(results.keys()[jj-1])
        overall_field_sensor_jj = result_ini['SensBox']

        # Extract current for every port for subsimulation jj
        i_jj = result_jj.GetSensor(result_jj.keys()[jj]).GetData('EM I(f)').GetComponent(0)      # CHECK SIM ORDER HERE ii+1/ii

        fieldclass_jj = overall_field_sensor_jj.GetData('EM E(x,y,z,f0)')
        Efield_jj = fieldclass_jj.Field(0)
        # Efield_norm_jj = (Efield_ii/(numpy.sqrt(P_jj)))#*2 #sqrt(4/3) #sqrt(2) #CHANGE POWER NORM
        Ex_jj = Efield_jj[:,0]
        Ey_jj = Efield_jj[:,1]
        Ez_jj = Efield_jj[:,2]

        E_combi = (Ex_ii.conj()*Ex_jj+Ey_ii.conj()*Ey_jj+Ez_ii.conj()*Ez_jj).flatten()

        E_combi_shaped = E_combi.reshape((new_shape[0],new_shape[1],new_shape[2]),order='F')

```

```
        R = 1/(i_ii*i_jj)*np.sum((sig_reshaped*E_combi_shaped*V_matrix).flatten()) # Calculate noise covariance

        R_matrix[ii-1,jj-1] = R[0] #Fill ii,jjth entry of noise covariance matrix



C_matrix = np.zeros([nports,nports],dtype='complex')
for ii in range(0,nports):
    for jj in range(0,nports):
        C_matrix[ii,jj] = R_matrix[ii,jj]/(np.sqrt(R_matrix[ii,ii])*np.sqrt(R_matrix[jj,jj])) # Calculate noise correlation from noise covariance

del fieldclass_jj, Efield_jj, Ex_jj, Ey_jj, Ez_jj, result_jj, Efield_ii, Ex_ii, Ey_ii, Ez_ii, result_ii, overall_field_sensor_ii, overall_field_sensor_jj
del fieldclass_ii, result_ini, overall_field_sensor_ini, fieldclass_ini, Efield_ini, Ex_ini, Ey_ini, Ez_ini, ld_ini

# path = r'D:\\Data\\SSAD - 1st Part\\Correlation Matrices\\' # Exporting path
# path = r'D:\\Data\\Loops - 2nd Part\\Correlation Matrices\\' # Exporting path
# path = r'D:\\Data\\Frac - 3rd Part\\Correlation Matrices\\' # Exporting path
path = r'D:\\Data\\DUKE - 4th Part\\Correlation Matrices\\' # Exporting path
mdict = {'C_matrix':C_matrix, 'R_matrix':R_matrix}
ext = '.mat'

savemat(path+'C_matrix'+' '+'24xSmallFracD_onDUKE'+ext,mdict)
```

B.5 SNR Calculation - Sim4Life

```
import s4l_v1 as s4l
from scipy.io import savemat
from scipy.io import loadmat
import s4l_v1.simulation.emfdtd as fdtd
import numpy as np

from numpy import linalg as LA
import XPostProcessor

#Load the R_matrix from an external path

```

```
# mat = loadmat(r'D:\Data\SSAD - 1st Part\Correlation Matrices\C_matrix 8xSSADtest')
# mat = loadmat(r'D:\Data\Loops - 2nd Part\Correlation Matrices\C_matrix 32xLoopsStraighttest')           # CHANGE LOAD PATH HERE
# mat = loadmat(r'D:\Data\Frac - 3rd Part\Correlation Matrices\C_matrix 8xFracD20mmtest')
mat = loadmat(r'D:\Data\DUKE - 4th Part\Correlation Matrices\C_matrix 24xSmallFracD_onDUKE')

R_matrix = mat.get(mat.keys()[0])

ents = s4l.model.AllEntities()

sims = list(s4l.document.AllSimulations)

ii = 0
sim = sims[ii]
results = sim.Results()
nports = 24

result = results.GetSimulation(results.keys()[0])

overall_field_sensor = result['SensBox']

B1 = overall_field_sensor['B1(x,y,z,f0)'] # Extract B1 Field

B1data = B1.Data # Contains grid and field (and other stuff)
B1grid = B1data.Grid
new_shape = (B1grid.Dimensions[0]-1, B1grid.Dimensions[1]-1, B1grid.Dimensions[2]-1)


B1field_normalized_all = np.zeros((new_shape[0]*new_shape[1]*new_shape[2],nports),dtype='complex')

# For-loop below extracts the B1minus-field for port n, and puts it as a column in an nvoxels*nports size matrix
for jj in range(1,nports+1):
    result = results.GetSimulation(results.keys()[jj-1])

    overall_field_sensor = result['SensBox']
    input_power_sensor = result['Input Power']

    i_in = result.GetSensor(result.keys()[jj]).GetData('EM I(f)').GetComponent(0)

    B1 = overall_field_sensor['B1(x,y,z,f0)'] # Extract B1
```

```
            Field

        B1data = B1.Data # Contains grid and field (and other stuff)
        B1grid = B1data.Grid # Select grid data
        xaxis = B1grid.XAxis
        yaxis = B1grid.YAxis
        zaxis = B1grid.ZAxis
        B1.Update() #?

        B1field_unshaped = np.array([B1data.Field(0)])

        B1field_normalized = (B1field_unshaped/i_in)

        new_shape = (B1grid.Dimensions[0]-1, B1grid.Dimensions[1]-1, B1grid.Dimensions[2]-1)

        B1field_normalized_all[:,jj-1] = B1field_normalized[:,:,1] #Select B1- here

R_matrix = np.matrix(R_matrix)

lengthall = new_shape[0]*new_shape[1]*new_shape[2]
SNRfield_flat = np.zeros(lengthall)
R_inv = LA.inv(R_matrix)

# For loop calculates the SNR per voxel
for ii in range(0,lengthall):
        B1row = np.matrix([B1field_normalized_all[ii,:]])
        B1row = np.transpose(B1row)
        B1rowherm = np.transpose(np.conj(B1row))
        SNRvoxel = np.sqrt(B1rowherm*R_inv*B1row)
        SNRvoxel = np.abs([SNRvoxel]) # Throws away very small imaginary part
        SNRfield_flat[ii] = SNRvoxel
SNRfield_flat = np.double(abs(SNRfield_flat))
SNR = SNRfield_flat#.reshape(new_shape)

# path = r'D:\\Data\\SSAD - 1st Part\\SNR Matrices\\'
# path = r'D:\\Data\\Loops - 2nd Part\\SNR Matrices\\'
# path = r'D:\\Data\\Frac - 3rd Part\\SNR Matrices\\' # Exporting path
path = r'D:\\Data\\DUKE - 4th Part\\SNR Matrices\\'
mdict = {'SNR':SNR,}
ext = '.mat'
savemat(path+'SNR_'+'24xSmallFracD_onDUKE'+ext,mdict)

del results
```

```
del result
```

References

[1] I.J. Voogt et al. Proceedings of the 23rd Annual ISMRM Scientific Meeting & Exhibition, Toronto, Canada, 2015;

[2] Haacke, E. (1999). Magnetic resonance imaging. 1st ed. New York: Wiley.

[3] Vlaardingerbroek, M. (2003). Magnetic resonance imaging. 3rd ed. Berlin: Springer.

[4] Hoult, D. I. "The Principle Of Reciprocity In Signal Strength Calculation - A Mathematical Guide". Concepts in Magnetic Resonance 12.4 (2000): 173-187. Web.

[5] Raaijmakers, A., Ipek, O., Klomp, D., Possanzini, C., Harvey, P., Lagendijk, J. and van den Berg, C. (2011). Design of a radiative surface coil array element at 7 T: The single-side adapted dipole antenna. Magnetic Resonance in Medicine, 66(5), pp.1488-1497.

[6] SEMCAD X Designer's Handbook - Reference Guide. (2012). 1st ed. Zurich, Switzerland: Schmid & Partner Engineering AG, pp.107-110.

[7] Homann, H., Graesslin, I., Eggers, H., Nehrke, K., Vernickel, P., Katscher, U., Dössel, O. and Börnert, P. (2012). Local SAR management by RF Shimming: a simulation study with multiple human body models. Magnetic Resonance Materials in Physics, Biology and Medicine, 25(3), pp.193–204.

[8] Katscher, U., Voigt, T., Findeklee, C., Vernickel, P., Nehrke, K. and Dossel, O. (2009). Determination of electric conductivity and local SAR via B1 mapping. Medical Imaging, IEEE Transactions on, 28(9), pp.1365–1374.

[9] Grissom, W., Yip, C., Zhang, Z., Stenger, V., Fessler, J. and Noll, D. (2006). Spatial domain method for the design of RF pulses in multicoil parallel excitation. Magnetic resonance in medicine, 56(3), pp.620–629.

[10] Homann, H. (2011). SAR prediction and SAR management for parallel transmit MRI. 1st ed. Karlsruhe: KIT Scientific Publ, pp.17–21.

[11] International Electrotechnical Commission (2015). Medical electrical equipment - Part 2-33: Particular requirements for the basic safety and essential performance of magnetic resonance equipment for medical diagnosis.

[12] Roemer, P.B., et al. "The NMR Phased Array". Magnetic Resonance in Medicine 16 (1990), 192-225.

[13] Raaijmakers AJE, van den Berg CAT. Antennas as surface array elements for body imaging at ultrahigh field strengths. eMagRes. 2012.

[14] Adriany, Gregor et al. "Transmit And Receive Transmission Line Arrays For 7 Tesla Parallel Imaging". Magnetic Resonance in Medicine 53.2 (2005): 434-445. Web.

[15] Vaughan, JT., Adriany, G. et al. "An efficient high frequency body coil for high field MRI". Magnetic Resonance in Medicine (2004); 52:851–859.

[16] Raaijmakers AJE, Lagendijk JJ, Klomp DJ, van den Bergen B, Possanzini C, Harvey PR, van den Berg CA. Boosting B1+ efficiency for RF transmit surface elements by a radiative antenna design. Proceedings of the 17th Annual ISMRM Scientific Meeting & Exhibition, Honolulu, HI, USA, 2009, 4764.

[17] Wiggins, GC, Zhang B, Lattanzi R, Chen G, Sodickson D. The electric dipole array: an attempt to match the ideal current pattern for central SNR at 7 tesla. Proceedings of the 20th Annual ISMRM Scientific Meeting & Exhibition, Melbourne, Australia, 2012; 2783

[18] Raaijmakers AJE, Voogt I, Klomp DWJ, Luijten PR, van den Berg CAT. Dipole antenna without ceramic substrate and still low SAR: the fractionated dipole antenna. Proceedings of the 21st Annual ISMRM Scientific Meeting & Exhibition, Salt Lake City, UT, USA, 2013; 4382

[19] Graessl, Andreas et al. "Design, evaluation and application of an eight channel transmit/receive coil array for cardiac MRI at 7.0T ". European Journal of Radiology (2011).

[20] Raaijmakers, A., Luijten, P. and van den Berg, C. (2015). Dipole antennas for ultrahigh-field body imaging: a comparison with loop coils. NMR in Biomedicine, p.n/a-n/a.

[21] Raaijmakers, Alexander J.E. et al. "The Fractionated Dipole Antenna: A New Antenna For Body Imaging At 7 Tesla". Magnetic Resonance in Medicine 75.3 (2015): 1366-1374. Web.

[22] Winter, L., Özerdem, C., Hoffmann, W., Santoro, D., Müller, A., Waiczies, H., Seemann, R., Graessl, A., Wust, P. and Niendorf, T. (2013). Design and Evaluation of a Hybrid Radiofrequency Applicator for Magnetic Resonance Imaging and RF Induced Hyperthermia: Electromagnetic Field Simulations up to 14.0 Tesla and Proof-of-Concept at 7.0 Tesla. PLoS ONE, 8(4), p.e61661.

[23] Metzger, Gregory J. et al. "Local B1+ Shimming For Prostate Imaging With Transceiver Arrays At 7T Based On Subject-Dependent Transmit Phase Measurements". Magnetic Resonance in Medicine 59.2 (2008): 396-409. Web.

[24] Wiggins GC. Mixing loops and electric dipole antennas for increased sensitivity at 7 Tesla. In: Proceedings of the 21st Annual ISMRM Scientific Meeting & Exhibition in Salt Lake City, Utah, USA, 2013, p2737.

[25] Wiggins GC, Zhang B, Lattanzi R, Sodickson D, inventors; New York University, assignee. Dipole array arrangement. US Patent WO2103159053A1, April 19, 2013.

[26] Lakshmanan K, Cloos M, Lattanzi R, Sodickson D, Novivkov D, Wiggins GC. The circular dipole. In: Proceedings of the 22nd Annual ISMRM Scientific Meeting & Exhibition in Milan, Italy, 2014.

[27] Lakshmanan K, Cloos M, Lattanzi R, Sodickson D, Wiggins GC. The loopole antenna: capturing magnetic and electric dipole fields with a single structure to improve transmit and receive performance. In: Proceedings of the 22nd Annual ISMRM Scientific Meeting & Exhibition in Milan, Italy, 2014.

[28] Lee W, Cloos MA, Sodickson D, Wiggins GC. Parallel Transceiver Array Design Using the Modified Folded Dipole for 7T Body Applications. In: Proceedings of the 21st Annual ISMRM Scientific Meeting & Exhibition in Salt Lake City, Utah, USA, 2013, p292.

[29] Nehrke, Kay and Peter Börnert. "DREAM-A Novel Approach For Robust, Ultrafast, Multislice B 1 Mapping". Magn Reson Med 68.5 (2012): 1517-1526. Web.

[30] Bevelacqua, P. (2015). Antenna-Theory.com - Field Regions. [online] Antenna-theory.com. Available at: http://www.antenna-theory.com/basics/fieldRegions.php [Accessed 15 Dec. 2015].